國立臺灣大學理學院物理學研究所

碩士論文

Department of Physics
College of Science
National Taiwan University
Master Thesis

銅鎳合金的熱、自旋、與電荷轉換研究

Study of Heat, Spin, and Charge Conversion in $Ni_{80}Cu_{20}$ Alloy

李文淵

Wen-Yuan Li

指導教授：黃斯衍 博士
曲丹茹 博士

Advisor: Dr. Ssu-Yen Huang
Dr. Danru Qu

中華民國 112 年 07 月

July 2023

doi:10.6342/NTU202302600

國立臺灣大學碩士學位論文
口試委員會審定書
MASTER'S THESIS ACCEPTANCE CERTIFICATE
NATIONAL TAIWAN UNIVERSITY

銅鎳合金的熱、自旋、與電荷轉換研究

Study of Heat, Spin, and Charge Conversion in Ni80Cu20 Alloy

本論文係李文淵(R09222067)在國立臺灣大學物理學系物理所完成之碩士學位論文，於民國 112 年 7 月 28 日承下列考試委員審查通過及口試及格，特此證明。

The undersigned, appointed by the Department / Institute of Physics on July 28, 2023 have examined a Master's thesis entitled above presented by Wen-Yuan Li (R09222067) candidate and hereby certify that it is worthy of acceptance.

口試委員 Oral examination committee:

董瑞安	田井基	
（指導教授 Advisor）		
林明吟		

系主任/所長 Director: 物理系系主任張貴峰

Acknowledgement

首先感謝指導教授黃斯衍博士及曲丹茹博士。

在進行實驗前期，感謝立信、昭偉協助測量儀器的建立。若不是他們的幫助，我的實驗沒辦法進行這麼順利。尤其特別感謝昭偉指導與修改分析數據用的程式。感謝勁佑說林昶滕 EPCR 給我精神上的支柱，讓我這篇致謝文多了一行。感謝 Tab Kool 告訴我在實驗室中，不論是實驗或是與老師的溝通，我都不是最慘的，讓我能夠珍惜現在我所擁有的好運。感謝首叡和我分享他各式各樣的威士忌和其知識，並且介紹他喜愛的酒吧，讓我在實驗進行中、結束後，或是壓力很大，抑或是心情不錯時有個可以喝酒的地方。感謝晉德替我接手了 cluster sputter 的管理，讓我卸下了管理高價且複雜又容易出事儀器的重擔。感謝林胤澤在 1 號機出狀況時總在第一時間處理，盡可能讓我的實驗進度不要被耽誤。感謝 蔣智傑 學長在我加入實驗室初期指導我在這個研究領域的必要知識，讓我以最快的速度進入狀況。同時也感謝他在實驗技巧上的指導，告訴我他自己的經驗，讓我少走許多歪路。除此之外，還感謝他教我如何購買股票，有了理財的概念，讓我不會每個月底都向立信借錢過活。感謝柏勳學長告訴我一些選股的知識及策略，像是要跟 蔣智傑 學長反著做就能賺錢，雖然目前還沒有實踐過。感謝實驗室不知名的前人所留下來的折疊床，讓我這一年睡實驗室時可以很舒適的睡在床上而不用睡地板。感謝宏益勸我碩一修古典力學錯過宇廷的場論，讓我避開了被當掉的結局。感謝允中把我從 monopole 的研究小組踢走讓我可以專心一志的做實驗。也感謝他傳授了咖啡可樂的配方(1:1 vol%)。感謝這三年咖啡與利他能的陪伴，讓我能夠在碩士期間專心做研究。

最後，謹以此文獻給我摯愛的雙親。

doi:10.6342/NTU202302600

中文摘要

在凝聚態物質研究領域中，通過自旋-軌道耦合(spin-orbit coupling)引起熱量、自旋和電荷明顯的相互轉換的材料引起了相當大的關注。特別感興趣的是為自旋電子學應用生成、檢測和操作自旋極化(spin polarized current)或純自旋電流(pure spin current)現象。通過操縱電子的自旋自由度，可以設計具有增強功能的自旋電子學器件。

已經研究了許多材料用於產生自旋電流，例如半導體、過渡金屬、拓撲半金屬等。對於過渡金屬而言，自旋霍爾角度(θ_{SH}, spin Hall angle)的數值由能帶結構決定，並且是特定金屬固有的。通常，過渡重金屬如鎢(W)和鉑(Pt)由於強自旋-軌道耦合而具有較大的電荷到自旋轉換。

在先前的研究中，探索了鎳銅(NiCu)合金與釔鐵石榴石($Y_3Fe_5O_{12}$,YIG)雙層結構中的自旋賽貝克效應(spin Seebeck effect)，發現在 Ni_xCu_{1-x} 合金中存在顯著自旋電荷轉換的增強現象，其歸因於自旋漲落(spin fluctuation)。值得注意的是，$Ni_{80}Cu_{20}$ 合金在順磁(paramagnetic)態下表現出極大的自旋霍爾角度，約為θ_{SH} = 46%，比鉑高出 4.5 倍，且其居裡溫度(Curie temperature)約為 300 K。通過減小薄膜厚度，由於有限尺寸效應(finite size effect)，$Ni_{80}Cu_{20}$ 薄膜從鐵磁(ferromagnetic)態過渡到順磁態。

在先前研究的基礎上，我們進一步研究了 $Ni_{80}Cu_{20}$ 合金在鐵磁態內熱、自旋和電荷的相互轉換。本研究特別探索了自旋霍爾磁阻(spin Hall magnetoresistance)和自旋能斯特熱電(spin Nernst induced thermal power)現象。此外，還對在 YIG 基板上得到 Pt 與 $Ni_{80}Cu_{20}$ 合金的結果進行了比較分析，以探討不同材料的熱自旋轉換效率與影響。

doi:10.6342/NTU202302600

Abstract

Materials that exhibit a pronounced inter-conversion of heat, spin, and charge through spin-orbit coupling have garnered considerable attention in the field of condensed matter research. Of particular interest is the generation, detection, and manipulation of spin polarized or pure spin current phenomenon for spintronics applications. By manipulating the spin degree of freedom of electrons, spintronic devices can be designed with enhanced functionality.

Many materials have been explored to generate spin current, such as semiconductors, transition metals, topological semimetals, and more. For the transition metals, the values of spin Hall angles (θ_{SH}) are dictated by the band structures and inherent to the specific metals. Usually, transition heavy metal such as W and Pt is known to have large charge to spin conversion due to strong spin-orbit coupling (SOC).

In previous study, the spin Seebeck effect in a Ni_xCu_{1-x}/YIG structure is explored, leading to the discovery of a significant enhancement in spin-to-charge conversion within the Ni_xCu_{1-x} alloy, attributed to spin fluctuations. Notably, the $Ni_{80}Cu_{20}$ alloy, characterized by a Curie temperature of approximately 300 K, exhibits

doi:10.6342/NTU202302600

an extraordinary large spin Hall angle of around $\theta_{SH} = 46\%$ in the paramagnetic state, surpassing Pt by 4.5 times. Through the reduction of film thickness, the $Ni_{80}Cu_{20}$ film undergoes a transition from the ferromagnetic (FM) state to the paramagnetic (PM) state due to the finite size effect.

Building upon the previous findings, we study further the inter-conversion of heat, spin, and charge within the $Ni_{80}Cu_{20}$ alloy in the FM state. This investigation specifically explores the spin Hall magnetoresistance (SMR) and spin Nernst induced thermal power (SNITP). Moreover, a comparative analysis is conducted between the results obtained from Pt and $Ni_{80}Cu_{20}$ alloys on YIG substrates to explore the thermal spin conversion efficiency and influence on different materials.

Keywords: spin current, spin Seebeck effect, spin Hall magnetoresistance, spin Nernst effect

doi:10.6342/NTU202302600

Contents

doi:10.6342/NTU202302600

doi:10.6342/NTU202302600

doi:10.6342/NTU202302600

doi:10.6342/NTU202302600

List of Figures

doi:10.6342/NTU202302600

doi:10.6342/NTU202302600

doi:10.6342/NTU202302600

doi:10.6342/NTU202302600

List of Tables

doi:10.6342/NTU202302600

doi:10.6342/NTU202302600

Chapter 1 Introduction

Spintronics has received much attention in condensed matter physics researches due to both scientific breakthroughs and technological advances, including short access time, low power consumption, and high endurance. In this area, electron spin, an intrinsic property of electron, plays an important rule due to additional state in a charge current, making electrical device more potential and providing a wider range of applications.

Spin is an intrinsic angular momentum carried by elementary and composite particles including electrons, neutrons, and atoms. It was found by the Stern–Gerlach experiment (Fig.1.1). During this experiment, silver atoms are emitted into an inhomogeneous magnetic field and their detection occurs at the rear end of the setup. If a particle possesses a magnetic moment arising from angular momentum within the atom, its trajectory varies based on the magnitude of the magnetic moment. On the contrary, if there is no magnetic moment, the particle follows a single trajectory. Since silver atom does not exist orbital angular momentum, it is considered to have no magnetic moment and follow one path. However it is observed that the atoms follow two distinct path, indicating the presence of an additional angular momentum, which is known as spin.

Similar to well-known physical quantities such as charge or energy, spin an-

doi:10.6342/NTU202302600

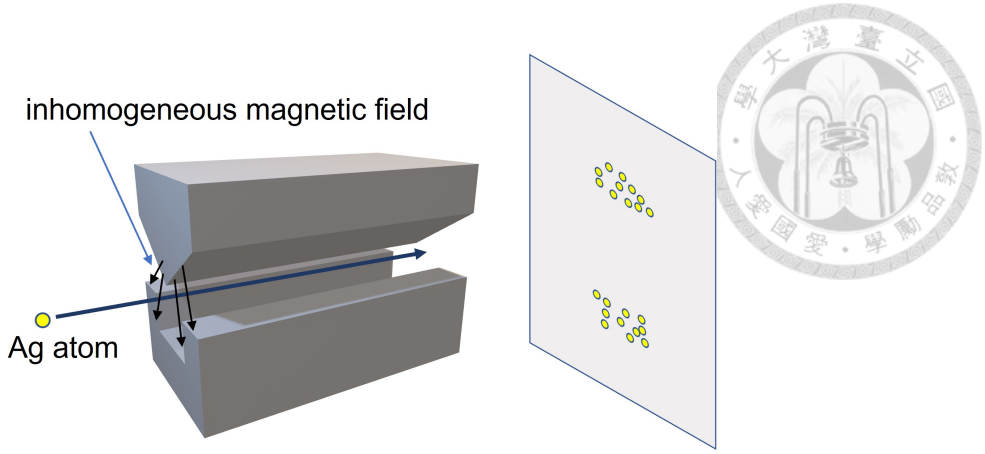

Figure 1.1: The schematic diagram for Stern–Gerlach experiment.

gular momentum transports by a flow called spin current (Fig.1.2). It is distinguished into two types: spin polarized current (Fig.1.2(b)) and pure spin current(Fig.1.2(c)). The former carries not only spins but also charge, while the latter carries only spin and no charge. In the case of pure spin current, the spin is considered to flow in opposite directions for opposite spins. To generate equal amount of spin, electrons in spin polarized current undergo more frequent scattering, resulting in a higher production of heat. Thus pure spin current brings a strong advantage in electrical device.

One notable application of spin current is magnetoresistive random-access memory (MRAM) [1, 2] (Fig.1.3). An MRAM consist of a thin (free) and a thick (fixed) magnetic layer, separated by a metallic (spacer) layer. The information is carried by the magnetic moment of the free layer and is read by means of giant magnetoresistance (GMR) phenomenon. The resistance of the device varies depending on whether the magnetic moment of the free layer is parallel or antiparallel

doi:10.6342/NTU202302600

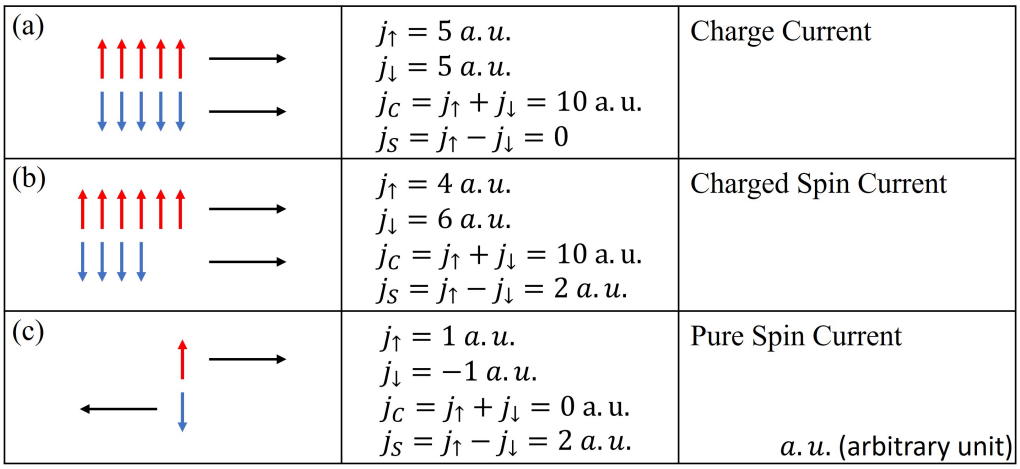

Figure 1.2: (a) Charge current, (b) spin polarized current, and (c) pure spin current

to that of the fixed layer. This difference in resistance is utilized for information detection. In the case of STT-MRAM, the state of the free layer is controlled (written) by the spin-transfer torque (STT) generated by spin polarized current. Applying a charge current, electrons whose spin parallel to magnetic moment in either free or fixed layer pass more easily, generating spin polarized current. When it is injected into the free layer, spin polarized current transfers its spin angular momentum to the magnetic moment, causing it to switch direction and change the state of the device. On the other hand, in SOT-MRAM, the free layer is controlled by spin-orbit torque (SOT), which is generated by pure spin current. Since it injects less charge current into the free layer, results in less electron scattering, the pure spin current provides the device with a longer service life and a higher number of operations.

With the advantage of high efficiency and low dissipation, pure spin current

doi:10.6342/NTU202302600

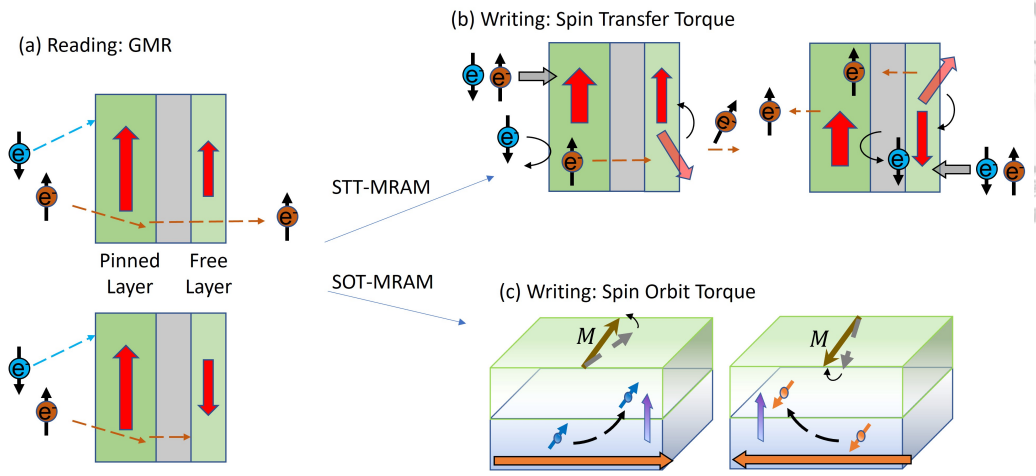

Figure 1.3: (a) Mechanism of reading process in MRAM, writing process in (b) STT-MRAM and (c) SOT-MRAM

generation becomes an important topic. Spin Hall effect, which is predicted by Dyakonov and Perel in 1971[3], convert charge current into spin current. One of the contribution arises from the scattering of electrons by scattering centers, resulting in the separation of electrons with different spins due to spin-orbit interactions, as Fig.1.4(a). Transition heavy metals such as Pt, Ta, W have been explored in the search of high efficiency of charge and spin conversion. Another contribution is intrinsic property of the material, which is understood after Jungwirth, Niu, and MacDonald [4]. They analyze the relationship between band structure (Fig.1.4(b)) and transverse conductivity in semiclassical transport theory which has

$$\sigma_{xy}^{z} = \frac{e}{\hbar}\sum_{k,n} f_{kn}\Omega_{n}^{z}(k)$$

$$\Omega_{n}^{z}(k) = \sum_{n',n} \frac{2\,\mathrm{Im}\{\,\langle kn|j_{x}^{z}|kn'\rangle\,\langle kn'|v_{y}|kn\rangle\}}{(\epsilon_{kn}-\epsilon_{kn'})^{2}}$$

where σ_{xy}^{z} represent the spin current parallel to y-axis with spin index parallel to

doi:10.6342/NTU202302600

z-axis under x-direction electric field, and Ω indicates the Berry curvature in the band structure. Taking it into account, some of topological semimetals such as TaAs[5], CoSi[6] are also attract attention.

Not only charge current produce spin current, heat flow also does. For specific magnetic insulators such as $Y_3Fe_5O_{12}$ (yttrium iron garnet, YIG), spin Seebeck effect generates magnonic spin current by a temperature gradient. It is observed in Pt/YIG bilayer structure by Uchida [7, 8]. By means of inverse spin Hall effect which convert spin current to charge current, spin current generated in YIG is injected into the Pt layer and detected in the form of electrical signal. Recently, researchers are interested in rare earth iron garnet for its magnetism and spin Seebeck effect [9]. On the other hand, due to the magnitude of converted charge current depend on conversion efficiency of metal layer, adopting various materials as the metal layer without changing magnetic insulator enables us to study their spin to charge conversion.

Heat flow also generates spin current in heavy metals. Spin Nernst effect, a

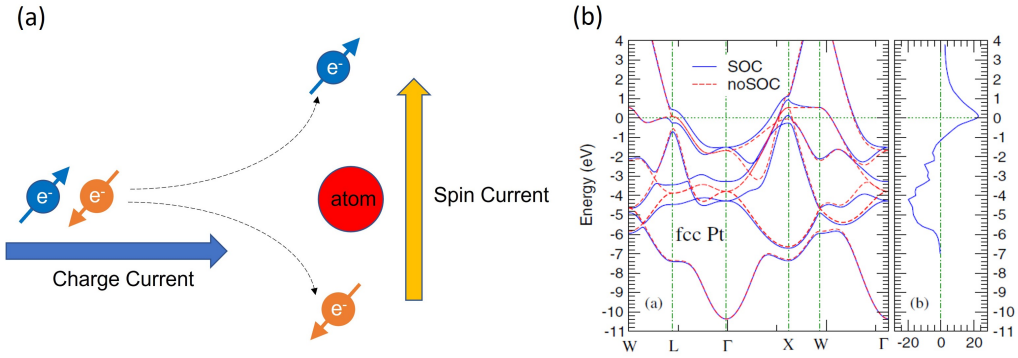

Figure 1.4: The schematic diagram for (a) extrinsic and (b) intrinsic spin Hall effect

doi:10.6342/NTU202302600

thermal version of spin Hall effect, convert heat flow into spin current. It is experimentally observed in W/CoFeB and Pt/YIG by Peng Sheng [10] and Meyer [11], separately. Spin current generated by spin Nernst effect interacts with magnetic moment at the interface, either incident into the magnetic layer or reflect back to heavy metal layer. With the large spin Hall angle in W and Pt, the reflected spin current is detected as an additional electrical signal. This mechanism implies that to study spin Nernst effect, it is necessary for the material to have a large spin Hall angle.

However, as large as spin Hall angle in Pt, the spin Nernst effect measurement results exhibit very small signal comparing with other spin Hall measurement. Because of experiment equipment limitation, the signal cannot increase by enhancing temperature gradient. Fortunately, it has known that Ni_xCu_{1-x} alloy has large Seebeck coefficient, which indicates the promise of high electrical signal through a relative low temperature gradient. In addition, by means of spin fluctuation during ferromagnetic phase transition, the spin current in Ni_xCu_{1-x} alloy can be enhanced, which is studied by Wu[12]. In this research, critical temperature is measured in each component of cooper. In addition, spin Hall angle is obtained by spin Seebeck measurement with Ni_xCu_{1-x}/YIG sample. It tells that the $Ni_{80}Cu_{20}$ has critical temperature at room temperature, having extremely large spin Hall angle of 11% in ferromagnetic (FM) state and 45% in paramagnetic (PM) state. With the size effect, adjusting the thickness can make $Ni_{80}Cu_{20}$ change between FM and PM states. This will be a promising material to study spin Nernst effect for these

doi:10.6342/NTU202302600

properties.

In this work, we confirm the spin Hall angle in FM $Ni_{80}Cu_{20}$/YIG by spin Hall magnetoresistance (SMR) measurement. The result is compared with Ni/Si and Pt/YIG. Additionally, spin Seebeck measurement is reproduced, in order to verify the sign of spin Hall angle. Furthermore, magnetic field dependent thermal voltage is measured to obtain the spin Nernst angle, which characterize the heat to spin conversion.

In the following content, we introduce in chapter 2 the basic concept of spin current and magnetism phenomena. In chapter 3, a detailed description on the sample preparation and measurement technique is addressed. The experiment result is included in chapter 4, where it shows the consistence of SMR and SSE result in FM $Ni_{80}Cu_{20}$, data analysis for spin Nernst effect measurement, and calculation of spin Nernst angle.

doi:10.6342/NTU202302600

doi:10.6342/NTU202302600

Chapter 2 Background

2.1 Basic Concepts

2.1.1 Spin Current Generation

The generation of spin currents involves the creation of a flow of spin angular momentum without the accompanying flow of charge. This process is fundamental in spintronics as it enables the exploitation of electron spins' unique properties in diverse devices. Several methods exist for generating spin currents, including the spin Seebeck effect [7, 8, 13], spin pumping [14], spin Hall effect [3, 15, 16], and spin Nernst effect [11, 10, 17, 18]. In this section, we focus on the introduction of spin Seebeck, spin Hall, spin Nernst, and spin Seebeck effects, which play significant roles in spin current generation and manipulation.

Spin Hall Effect (SHE)

The spin Hall effect (SHE) occurs when a charge current is applied, leading to the separation and flow of electrons with different spin states in opposite directions perpendicular to the original current [3, 15, 16]. This phenomenon results in the generation of a spin current, as depicted in Fig.2.1. The SHE is attributed to three mechanisms: skew scattering, side jump, and intrinsic mechanisms. It provides

doi:10.6342/NTU202302600

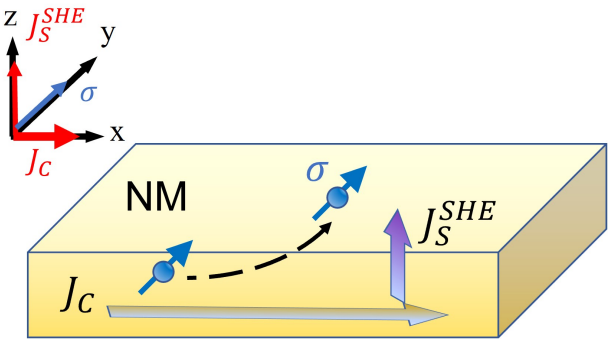

Figure 2.1: The schematic diagram of spin Hall effect. A charge current J_C flows along x-axis, which generates a spin current J_S^{SHE} that flows in z-axis with spin index σ pointed along y-axis.

a convenient method for generating pure spin currents in various technological applications.

The spin current generated by the spin Hall effect can be determined using the following equation:

$$J_S = \theta_{SH} \frac{\hbar}{2e} J_C \times \sigma \tag{2.1}$$

In this equation, J_S represents the spin current, J_C denotes the charge current, θ_{SH} corresponds to the spin Hall angle, which characterizes the efficiency of converting charge currents to spin currents, and σ indicates the spin index that denotes the direction of spins. Evaluating the spin Hall angle in different materials is a significant research focus within the field of spin Hall effect since it helps determine a material's ability to convert charge currents into spin currents.

doi:10.6342/NTU202302600

Spin Nernst Effect (SNE)

The spin Nernst effect is thermal version of SHE that separating electrons with different spin states in opposite directions perpendicular to the heat flow [11, 10, 17, 18]. The phenomena results in the generation of a transverse spin current, as shown in Fig.2.2. The spin current generated by the SNE can be described by

$$J_S = \theta_{SN} \frac{\hbar}{2e} \frac{S}{\rho} (-\nabla T) \times \sigma \tag{2.2}$$

Here, J_S represents the spin current, S denotes the Seebeck coefficient, θ_{SN} represents the spin Nernst angle, which characterizes the efficiency of heat-to-spin conversion, and σ represents the spin index indicating the direction of spins. Determining the spin Nernst angle in different materials is a significant focus of research within the field of spin Nernst effect, as it helps characterize the material's ability to convert heat flow into spin currents.

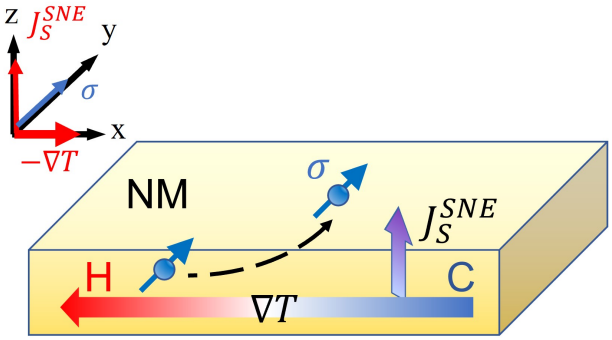

Figure 2.2: The schematic diagram of spin Nernst effect. A temperature gradient ∇T flows along x-axis, which generates a spin current J_S^{SNE} that flows in z-axis with spin index σ pointed along y-axis.

doi:10.6342/NTU202302600

Spin Seebeck Effect (SSE)

In spin Seebeck magnetic insulators, the spin Seebeck effect arises when a temperature gradient is present, resulting in the generation of a spin current that aligns with the temperature gradient [7, 8, 13]. When a temperature gradient is applied to this type of materials, thermal energy is transferred, causing the excitation of magnons. These thermally excited magnons carry spin angular momentum that aligns with the magnetization direction in the ferromagnetic material, thereby generating a spin current. The relationship between the direction of heat flow, spin current, and spin index is illustrated in Fig.2.3.

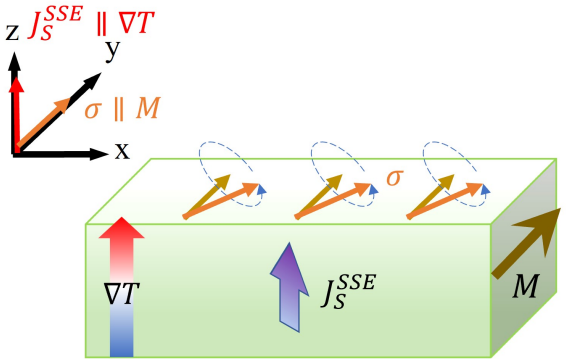

Figure 2.3: The schematic diagram of spin Seebeck effect. A temperature gradient ∇T is applied along the z-axis, resulting in the generation of a spin current J_S^{SSE} that flows parallel to ∇T. The spin current J_S^{SSE} possesses a spin index σ aligned with the magnetization M along the y-axis.

doi:10.6342/NTU202302600

2.1.2 Spin Current Detection

Despite the various methods available to generate spin currents, directly detecting spin angular momentum remains a challenge. Unlike charge and heat, which can be measured using ammeters, voltmeters, and thermometers, there are no direct tools to detect angular momentum. However, an indirect approach to spin detection can be achieved through the use of bilayers. By converting the spin current into a measurable form, it becomes feasible to confirm the presence or absence of spin currents.

Inverse Spin Hall Effect (ISHE) for Spin Detection

The inverse spin Hall effect (ISHE) [19, 20] is a powerful technique employed in spin detection. It allows the conversion of spin currents back into charge currents, which can then be readily measured using conventional electrical detection methods. The ISHE arises from the spin-orbit coupling in non-magnetic materials, where an incident spin current induces a transverse charge voltage across the material. This voltage is proportional to the magnitude of the spin current, enabling the detection and quantification of spin currents.

Contrary to the spin Hall effect (SHE), which generates a spin current from a charge current, the ISHE converts a spin current back into a charge current, as illustrated in Figure 2.3. It is important to note that the efficiency of the SHE and ISHE is same. Thus, the charge current transformed from the spin current follows

doi:10.6342/NTU202302600

the relationship:

$$J_C = \theta_{SH}\frac{2e}{\hbar}J_S \times \sigma \tag{2.3}$$

where J_C represents the charge current, J_S is the spin current, θ_{SH} is the spin Hall angle, which characterizes the efficiency of spin-to-charge conversion, and σ represents the spin index indicating the direction of spins.

The ISHE provides a crucial link between the generation of spin currents and their detection through electrical measurements. By exploiting the ISHE, we can indirectly probe the presence and characteristics of spin currents, enabling the study of spin transport phenomena and the development of spin-based devices.

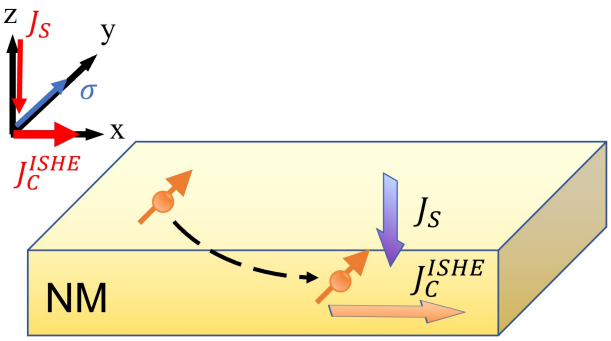

Figure 2.4: The schematic diagram of inverse spin Hall effect. A spin current J_S flows along $-z$-axis with spin index σ pointed along y-axis, generating a charge current J_C^{ISHE} that flows in x-axis.

Spin Seebeck Effect (SSE) Measurement

One significant application of spin detection using the inverse spin Hall effect (ISHE) is in the measurement of the spin Seebeck effect. The spin Seebeck effect involves the conversion of a temperature gradient into a spin current in magnetic

doi:10.6342/NTU202302600

materials. By placing a non-magnetic material adjacent to the magnetic material, the spin current generated by the spin Seebeck effect can be detected using the ISHE in the non-magnetic layer, as Fig.[2.5]. The ISHE signal can be described by the relationship [13]:

$$\frac{E_{\text{ISHE}}}{2\nabla T} = C\rho(t)\theta_{SH}\frac{\lambda_S}{t}\tanh\left(\frac{t}{2\lambda_S}\right) \tag{2.4}$$

Here, E_{ISHE} is the voltage due to the ISHE, ∇T is the temperature gradient, C is the spin current injection coefficient, $\rho(t)$ and t represent the resistivity and thickness of the detector layer, θ_{SH} is the spin Hall angle, and λ_S is the spin diffusion length. The coefficient C incorporates various factors such as the gyromagnetic ratio (γ), finite ferromagnetic insulator thickness factor (ρ'), maximum wavenumber (k_m), magnon diffusion length (l_m), saturation magnetization (M_S), parameters from the diffusion equation (B_1, B_S, and B_2), spin mixing conductance ($g_{\text{eff}}^{\uparrow\downarrow}$), and the Boltzmann constant (k_B).

By analyzing the resulting charge current, researchers can extract valuable information regarding the magnitude and direction of the spin current induced by the spin Seebeck effect. This measurement approach, utilizing the ISHE, enables the study and characterization of spin currents generated by the spin Seebeck effect, contributing to advancements in spin-based energy conversion and information processing.

doi:10.6342/NTU202302600

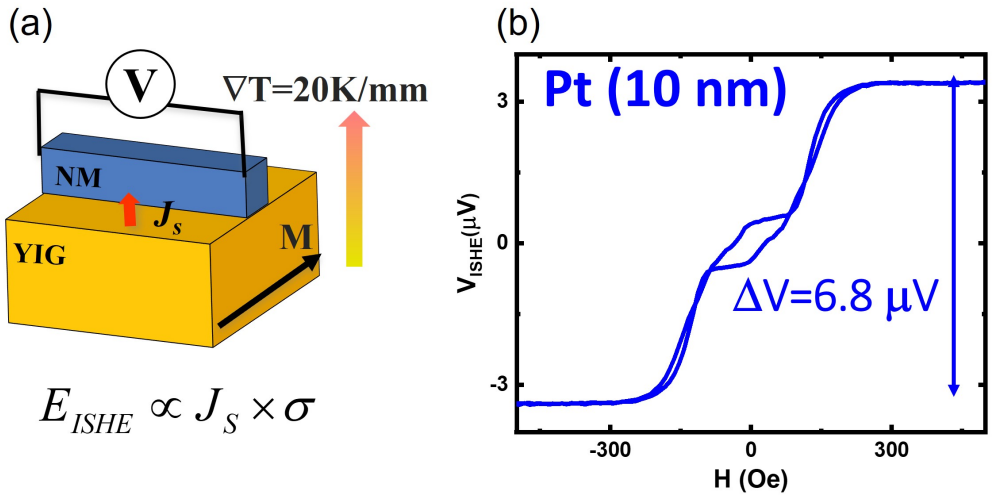

Figure 2.5: Spin Seebeck Measurement. (a)Schematic diagram of the SSE measurement. Spin current generated by SSE in YIG inject into NM layer. A transverse voltage converted by ISHE can be detected. (b)SSE measurement result of Pt(10 nm)/YIG [21]

2.2 The $Ni_{80}Cu_{20}$ alloy

In recent years, there has been extensive research on charge-to-spin conversion (spin Hall effect, SHE). However, heat-to-spin conversion (spin Nernst effect, SNE) has received less attention due to the challenges associated with its measurement.

To address the detection of spin currents generated by SNE, it is essential to employ a detection layer with a large spin Hall angle. Notably, recent investigations have unveiled a remarkable enhancement of spin-to-charge conversion in Ni_xCu_{1-x} alloys, attributed to spin fluctuation effects [12]. Specifically, the $Ni_{80}Cu_{20}$ alloy, with a Curie temperature of approximately 300K, exhibits an ex-

doi:10.6342/NTU202302600

ceptionally large spin Hall angle of about $\theta_{SH} = 45\%$ in its paramagnetic state. This value is 4.5 times larger than that of Pt. Even in the ferromagnetic state, the $Ni_{80}Cu_{20}$ alloy still maintains a substantial spin Hall angle of $\theta_{SH} = 12\%$, as depicted in Figure 2.6. The significant enhancement of the spin Hall angle in Ni_xCu_{1-x} alloys makes them promising candidates for amplifying the spin Nernst effect signal, facilitating easier measurement.

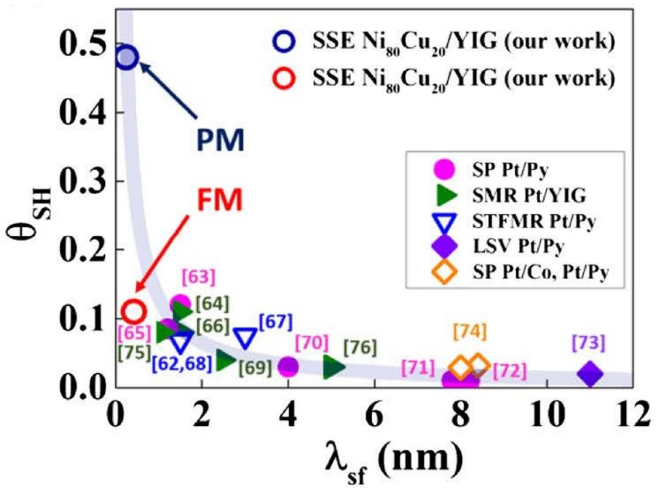

Figure 2.6: Integration of reported spin Hall angle for Pt. The blue and red open circles are the result for Ni_xCu_{1-x} in the PM and FM state [12]. Other symbols are the result for Pt reported by several groups with various measuring methods. The product of spin Hall angle and spin diffusion length from the result of each group is roughly equal.

Thus, the Ni_xCu_{1-x} alloy with its large spin Hall angle offers great potential for advancing the detection of the spin Nernst effect. Its unique properties, including the enhanced spin-to-charge conversion and robust performance in both paramagnetic and ferromagnetic states, make it a promising material for studying and harnessing the spin Nernst effect.

doi:10.6342/NTU202302600

2.3 Spin Transport Theory Driven by J_C and ∇T

In the preceding section, we introduced the concepts of spin Hall effect, spin Nernst effect, and their respective angles (θ_{SH} and θ_{SN}) as convenient measures of the spin current direction. However, it is important to note that 'J_S' as a vector does not fully characterize the direction of spin. As a result, it becomes challenging to establish a comprehensive spin transport theory based solely on this simplified representation. In this section, we follow the reference [22] and consider the spin current as a tensor:

$$j_{Sij} = \frac{en}{2}\{\sigma_i, v_j\}; \quad i, j \in \{x, y, z\} \tag{2.5}$$

j_{Sij} means the carriers with spin σ pointing along direction i towards direction j. Furthermore, the spin transport theory for metallic systems in contact with a magnetic insulator using a drift-diffusion model can be derived. This theoretical framework will enable us to understand the behavior of spin currents under the influence of charge currents and temperature gradients.

2.3.1 Theory of Spin Hall Magnetoresistance

We discuss the composition of spintronic devices, which typically involve the integration of non-magnetic (NM) and magnetic materials to enable precise manipulation of the spin state. Recently, magnetic insulators, particularly yttrium iron garnet (YIG), have garnered significant attention in this field due to their advantageous properties, including no shunting effects and low magnetization damping.

doi:10.6342/NTU202302600

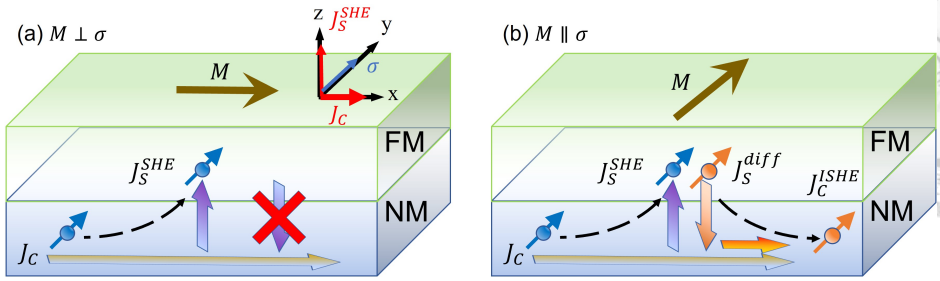

Figure 2.7: Schematic diagram of spin Hall magnetoresistance mechanism. Resistance in a NM/FM bilayer depends on direction of magnetization on FM. (a) shows the $M \perp \sigma$ case that spin accumulation does not diffuse back, which has larger value of resistance than (b) the $M \parallel \sigma$ case due to the addition current generated by ISHE.

In heterostructures comprising a NM layer and a ferromagnetic (FM) material, a specific type of magnetoresistance arises. Spin current generated by the spin Hall effect (SHE) in the NM layer flows perpendicular to the charge current, resulting in the accumulation of spins at the NM/FM interface. The direction of the FM's magnetic moment, which can be controlled by an external magnetic field, determines whether the spin current diffuses back into the NM layer or not. When the magnetic moment is aligned parallel to the spin, the spin current diffuses back, generating an additional charge current in the NM layer through the inverse spin Hall effect (ISHE). This additional current effectively reduces the resistance in the system. Combining the SHE and ISHE phenomena, this magnetoresistance originates from the spin current generated in the NM layer and is referred to as spin Hall magnetoresistance (SMR) [23]. The mechanism is shown in Fig.2.7.

The drift-diffusion model is widely accepted as the most plausible theory for

doi:10.6342/NTU202302600

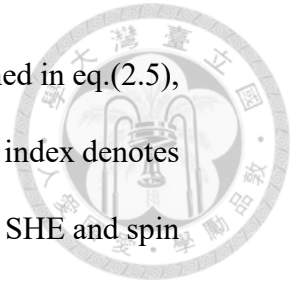

explaining the SMR phenomenon, as described in [22]. As mentioned in eq.(2.5), the first index of j_{Sij} represents the spin direction, while the second index denotes the direction of spin current flow. This spin current is driven by the SHE and spin accumulation at the boundary.

Assuming isotropic spin Hall conductivity in the NM layer, the spin current can be expressed as:

$$j_{Sij} = -\frac{\sigma_C}{e}(\theta_{SH}\varepsilon_{ijk}\partial_k\mu_0 + \frac{1}{2}\partial_j\mu'_{Si}) \tag{2.6}$$

Here, σ_C represents the conductivity, μ_0 is the charge-dependent chemical potential, and μ'_{Si} represents the spin-dependent chemical potential. The first term in the equation describes the SHE, while the second term indicates the diffusion of spin accumulation. By treating the gradients of μ as electric fields, the equation can be rewritten as $j_{Sij} = \sigma_C(\theta_{SH}\varepsilon_{ijk}E_k + E_{eff,ij})$. The first term is comparable to the equation (2.1). Furthermore, the components of μ'_{Si} can be interpreted as spin-dependent energies with corresponding spin directions, incorporating both charge and spin contributions. Thus, it is useful to define the chemical potential with only spin contribution as $\mu_{Si} = \mu'_{Si} - \mu_0$, which is commonly known as spin accumulation.

On the other hand, the charge current consists of the original current driven by an external electric field and an additional component induced by the ISHE. It can be expressed as:

$$j_{Ci} = -\frac{\sigma_C}{e}(\partial_i\mu_0 - \frac{1}{2}\theta_{SH}\varepsilon_{ijk}\partial_j\mu'_{Sk}) \tag{2.7}$$

doi:10.6342/NTU202302600

By determining the distribution of charge and spin accumulation, the relationship between charge and spin currents can be established.

The spin accumulation can be obtained from the diffusion equation:

$$\nabla^2 \mu_S = \frac{\mu_S}{\lambda_S^2} \tag{2.8}$$

Here, λ_S represents the spin diffusion length, which characterizes the distance over which the spin state of electrons can be maintained. Consider a bilayer system consisting of a NM and FM insulator, with an electric field applied in the x direction, as shown in Figure 2.7. For the NM film with a thickness of d_N in the z direction, and by imposing the boundary conditions $j_{Siz}(d_N) = 0$ and $j_{Siz}(0) = j_{Siz}^{(F)}$ (where $j_{Siz}^{(F)}$ is the spin current between the interface), the equation can be solved. Substituting it into equation (2.7) allows us to determine the charge current and subsequently derive the resistivity:

$$\rho_{xx} = \left(\frac{\bar{j_{Cx}}}{E_x}\right)^{-1} = \rho + \Delta\rho_0 + \Delta\rho_1(1 - m_y^2) \tag{2.9}$$

$$\rho_{xy} = \frac{\bar{j_{Cy}}}{\sigma_C^2 E_x} = \Delta\rho_1 m_x m_y + \Delta\rho_2 m_z \tag{2.10}$$

where

$$\frac{\Delta\rho_0}{\rho} = -\theta_{SH}^2 \frac{2\lambda_S}{d_N} \tanh\frac{d_n}{2\lambda_S} \tag{2.11}$$

$$\frac{\Delta\rho_1}{\rho} = \theta_{SH}^2 \frac{\lambda_S}{d_N} \mathrm{Re}\left\{\frac{2\lambda_S G_{\uparrow\downarrow} \tanh^2 \frac{d_N}{2\lambda_S}}{\sigma_C + 2\lambda_S G_{\uparrow\downarrow} \coth\frac{d_n}{\lambda_S}}\right\} \tag{2.12}$$

$$\frac{\Delta\rho_2}{\rho} = -\theta_{SH}^2 \frac{\lambda_S}{d_N} \mathrm{Im}\left\{\frac{2\lambda_S G_{\uparrow\downarrow} \tanh^2 \frac{d_N}{2\lambda_S}}{\sigma_C + 2\lambda_S G_{\uparrow\downarrow} \coth\frac{d_n}{\lambda_S}}\right\} \tag{2.13}$$

Here, ρ denotes the intrinsic electric resistivity of the NM layer. Equation (2.9) indicates that the resistivity changes when the magnetic moment in the FM layer

doi:10.6342/NTU202302600

is oriented in the y direction, parallel to the spin generated by the SHE in the NM layer. This demonstrates the magnetoresistance caused by the SHE. Additionally, equation (2.10) suggests that the SHE also induces the planar and anomalous Hall effects, which exhibit similar phenomena to those observed in magnetic materials.

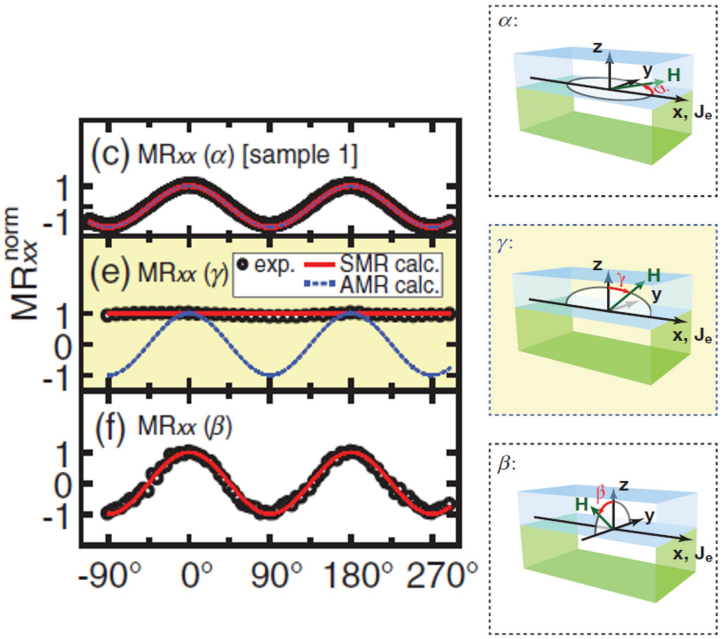

Figure 2.8: SMR for Pt/YIG measured by [23]. α is the angle between magnetic field and x-axis, andβ, γ are the angle between field and z-axis. The absence of a γ scan signal and the presence of a β scan signal shows that MR originate from spin Hall effect.

The same research group also conducted measurements of the Spin Hall effect in Pt [23]. In their experiment, Pt was used as the NM layer, while YIG served as the FM layer. Direction of the applied magnetic field was systematically varied in the xy plane (referred to as α scan, where α is the angle between magnetic field and x-axis), xz plane (γ scan, where γ is the angle between field and z-axis), and yz plane (β scan, where β is the angle between magnetic field and z-axis). The

doi:10.6342/NTU202302600

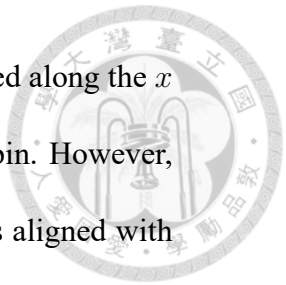

resistance remained unchanged when the magnetic field was oriented along the x and z directions, indicating the absence of an effect related to the spin. However, a decrease in resistance was observed when the magnetic field was aligned with the y direction, which coincides with the direction of the spin. This observation supports the occurrence of the spin Hall effect in the NM layer, as deduced from the aforementioned results. It is worth noting that the absence of a γ scan signal and the presence of a β scan signal provide additional evidence for the spin Hall effect occurring in the NM layer, as mentioned in eq.(2.9)

2.3.2 Theory of Spin Nernst Induced Thermal Power (SNITP)

Similar to the SMR, the spin current generated by the SNE can be detected using NM/FM heterostructures. In contrast to the SHE, the SNE generates spin current in response to a temperature gradient rather than a charge current. When the magnetic moment is parallel to the spin direction, the spin accumulation at the interface diffuses back into the NM layer. This diffusion of spin accumulation induces a charge current through the ISHE, resulting in the generation of an additional voltage. We refer to this voltage as spin Nernst-induced thermal power (SNITP). The mechanism is illustrated in Figure 2.9.

Calculations of SNITP have also been reported by [24, 25]. The spin current in the NM layer consists of contributions from the SNE and the diffusion of spin accumulation, while the charge current includes contributions from the Seebeck

doi:10.6342/NTU202302600

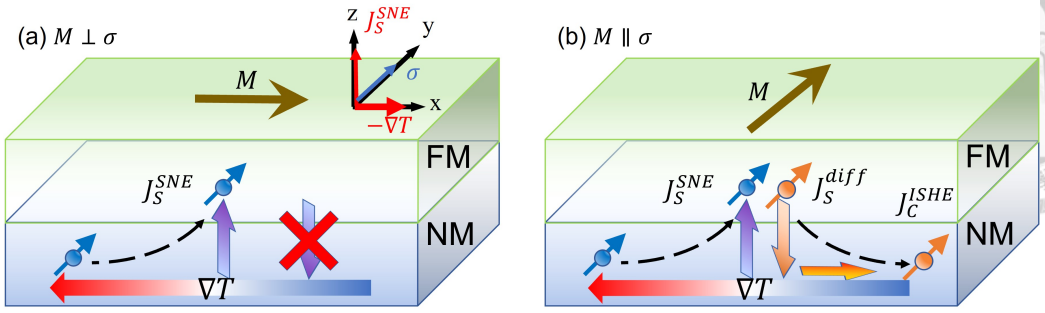

Figure 2.9: Schematic diagram of spin Nernst effect induced thermal power mechanism. Thermal voltage in a NM/FM bilayer depends on direction of magnetization on FM. (a) shows the $M \perp \sigma$ case that spin accumulation does not diffuse back, which has different value of thermal voltage with (b) the $M \parallel \sigma$ case due to the additional current generated by ISHE.

effect and the ISHE. The former can be written as:

$$j_{Sij} = j_{SNE,ij} - \frac{\sigma_C}{2e}\partial_j \mu'_{Si} \tag{2.14}$$

Here, $j_{SNE,ij} = \theta_{SN}\sigma_C S_N \varepsilon_{ijk}\partial_k T = -\frac{\sigma_C}{e}\theta_{SN}\varepsilon_{ijk}\partial_k \mu_0$ represents the drift spin current, and S_N corresponds to the Seebeck coefficient. On the other hand, the charge current driven by the thermal electromotive force and the additional component induced by the ISHE has the same form as the equation (2.7).

Considering the same system as in the SMR case, with a temperature gradient applied in the x direction, as shown in Figure 2.9, and using the same boundary condition at the interface, the magnetic moment dependent Seebeck coefficient can be expressed as:

$$S_{xx} = -\frac{\bar{j_{Cx}}}{\sigma_C \partial_x T} = S_N + \Delta S_0 + \Delta S_1 (1 - m_y^2) \tag{2.15}$$

doi:10.6342/NTU202302600

$$S_{xy} = \Delta S_1 m_x m_y + \Delta S_2 m_z \tag{2.16}$$

where

$$\Delta S_0 = \theta_{SN}\theta_{SH} S_N \frac{2\lambda_S}{d_N} \tanh \frac{d_N}{2\lambda_S} \tag{2.17}$$

$$\Delta S_1 = -\theta_{SN}\theta_{SH} S_N \frac{\lambda_S}{d_N} \mathrm{Re}\left\{ \frac{2\lambda_S G_{\uparrow\downarrow} \tanh^2 \frac{d_N}{2\lambda_S}}{\sigma_C + 2\lambda_S G_{\uparrow\downarrow} \coth \frac{d_n}{\lambda_S}} \right\} \tag{2.18}$$

$$\Delta S_2 = \theta_{SN}\theta_{SH} S_N \frac{\lambda_S}{d_N} \mathrm{Im}\left\{ \frac{2\lambda_S G_{\uparrow\downarrow} \tanh^2 \frac{d_N}{2\lambda_S}}{\sigma_C + 2\lambda_S G_{\uparrow\downarrow} \coth \frac{d_n}{\lambda_S}} \right\} \tag{2.19}$$

Again, we see the SNE induced planar and anomalous Nernst effects in equation (2.16).

A study by [10] reported the SNE results for tantalum (Ta) and tungsten (W). The y-direction field dependent thermal voltage with x-direction temperature gradient results are shown in Fig.2.10. The SNE signal observed in W was approximately 0.5 μV, which, although seemingly large, is much smaller compared to the SHE signal ($\sim$ 312 μV) obtained from samples of the same size. In Ta samples, the SNE signal was barely detectable.

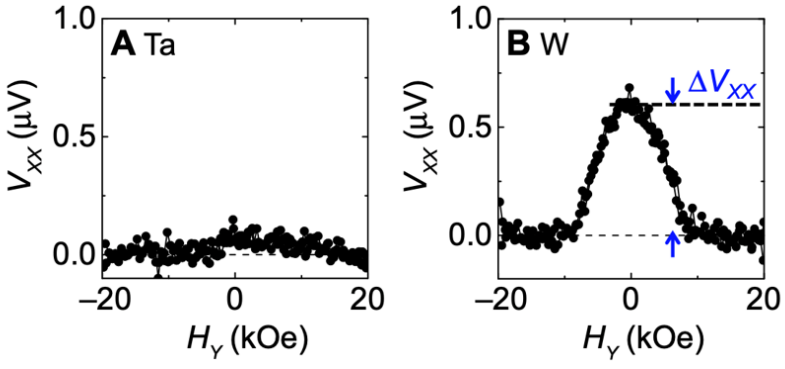

Figure 2.10: Field dependent result of spin Nernst effect in (A) Ta and (B) W [10].

doi:10.6342/NTU202302600

Another study of SNITP is also measured with Pt/YIG [11]. Fig.2.11 shows the angle scan result, which clearly reveals an even smaller β signal of only 0.05 μV and a noise-like γ signal. This demonstrates that the spin current is generated by a temperature gradient in the Pt layer. Moreover, the obtained spin Nernst angle ($\theta_{SN} = -20.0\%$) is consistent with their result from first-principle calculations.

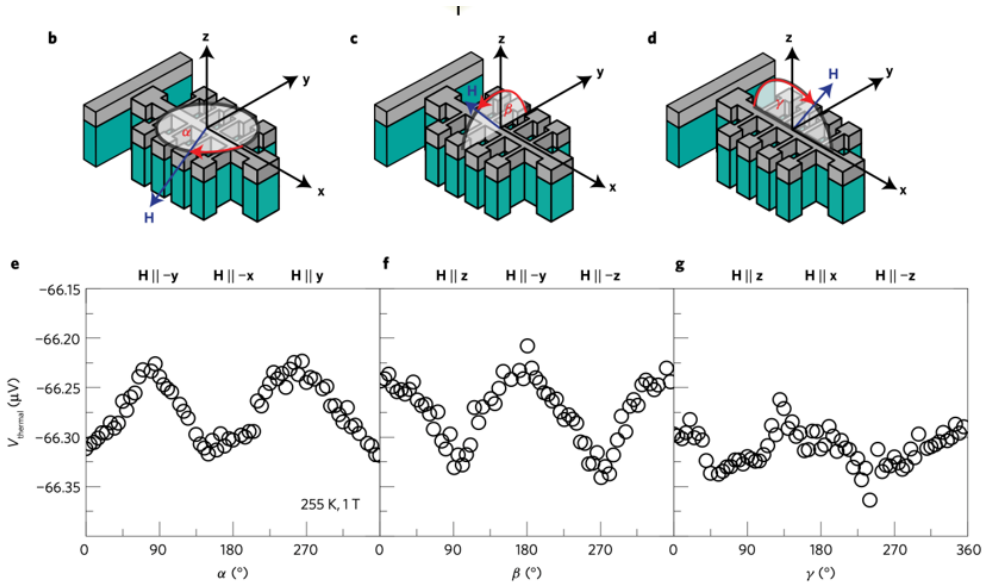

Figure 2.11: Angle dependent result of spin Nernst effect in Pt by [11].

2.4 Phenomena in Magnetic Material

Magnetic materials exhibit a wide range of intriguing phenomena that play a crucial role in spintronics and related fields. In this section, we will explore some of these phenomena, including magnetism, anisotropic magnetoresistance (AMR), the anomalous Hall effect (AHE), and the anomalous Nernst effect (ANE). Understanding these phenomena is essential for harnessing the unique properties of

doi:10.6342/NTU202302600

magnetic materials in spintronic devices.

2.4.1 Magnetism

Magnetism is a fundamental property exhibited by certain materials, arising from the presence of magnetic moments associated with their atomic or molecular structure. These magnetic moments can align in different behaviors with external magnetic field, leading to various types of magnetism. The relation between field and the alignment can be written as

$$\vec{M} = \chi \vec{H}$$

where $\vec{M}$ is magnetization which represent magnetic moment per unit volume, and χ is susceptibility which measures that how much a material will become magnetized in an applied field. The most common classifications of magnetism are diamagnetism, paramagnetism, ferromagnetism, antiferromagnetism, and ferrimagnetism. The magnetization schematic diagrams are shown in Fig.2.12, and the detail will be introduced.

Diamagnetism

Diamagnetism presents in all materials, and always makes a weak contribution to the response to a magnetic field. It results in a net magnetization of zero with the absent of field, and tends to produce an opposite direction of magnetization when the field applied. This behavior is known to arise from the orbital motion of electrons around the nucleus, which can be treated as tiny current loop. With

doi:10.6342/NTU202302600

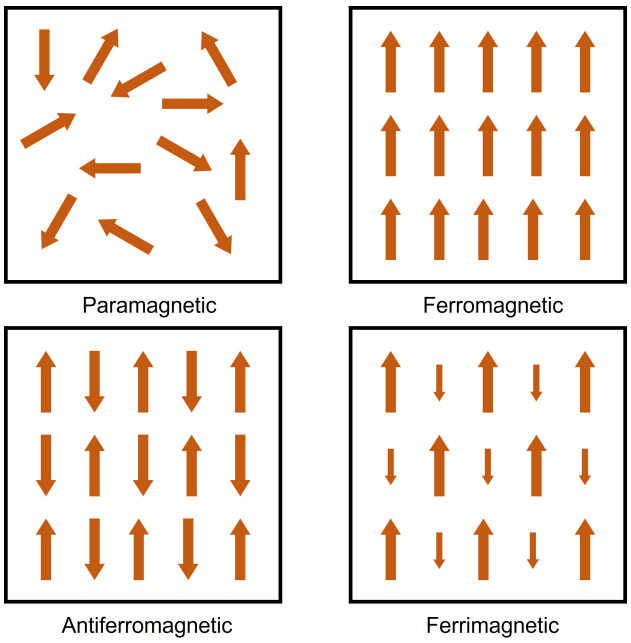

Figure 2.12: Schematic diagram for different types of magnetism

Larmor precession frequency $\omega = eB/2m_e$, this current can be written as

$$I = -\frac{Ze^2B}{2\pi m}$$

and lead to

$$\chi = -\frac{\mu_0 e^2 Z n}{6m} \left\langle r^2 \right\rangle \tag{2.20}$$

which is known as Langevin susceptibility. Z in the equation is atomic number, and n is the number of atoms per unit volume. From the negative sign, we can see the opposite direction contribution of magnetization. Note that Langevin susceptibility is temperature independent and only considers the contribution from fully filled electron shell. Also note that diamagnetism is so weak that often be obscured when other forms of magnetism (such as ferromagnetism or paramagnetism) are present.

doi:10.6342/NTU202302600

The Langevin theory is not the full picture for metals because there are also non-localized electrons. Landau predicted that there is an additional contribution

$$\chi = -\frac{1}{3}\mu_0\mu_B^2\left(\frac{3n}{2E_F}\right) \tag{2.21}$$

which is based on free electron gas in conductors. Again, this is temperature independent in the case of three-dimension.

Paramagnetism

Paramagnetism is a form of magnetism exhibited by certain materials that possess unpaired electrons. Unlike diamagnetic materials, paramagnetic materials are weakly attracted to magnetic field. The presence of unpaired electrons gives rise to a net magnetic moment within the material, which aligns with the applied magnetic field.

In paramagnetic materials, the unpaired electrons have non-zero spins, which has net magnetic moment. With the absent of magnetic field, the magnetic moments of these unpaired electrons direct randomly, therefore the magnetization is zero. When an external field is applied, these moments align with the field, leading to a net magnetization in the same direction as the applied field. However, the alignment is relatively weak and can be easily disrupted by thermal energy. The result finally is that only part of moments align along the direction of field, and therefore the susceptibility is positive but weak. This behavior can be describe as Curie's law: $\chi = \frac{C}{T}$, which has a considerable dependence with temperature.

doi:10.6342/NTU202302600

In microscopic point of view, a statistical model has been proposed by Pauli. Moments in the materials contain those parallel and anti-parallel to magnetic field, which have opposite sign of Zeemzan energy and present different distribution. In high temperature, this leads to the approximation of magnetization

$$M \simeq \frac{n\mu_B^2 H}{kT} \tag{2.22}$$

and again see the Curie's law. This model is apply to the elements with total angular momentum number $J = \frac{1}{2}$ such as some alkaline metal. Other materials with different J can be easily modified.

Ferromagnetism

Different from diamagnetism and paramagnetism, ferromagnetic materials exhibit a unique behavior known as long-range ordering at the atomic level. This ordering arises due to the exchange interaction between the unpaired electron spins of neighboring atoms, leading to the formation of magnetic domains. Within each domain, the magnetic moments align in the same direction, resulting in a net macroscopic magnetization.

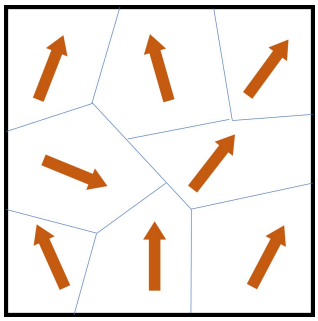

Figure 2.13: Schematic diagram for magnetic domain

doi:10.6342/NTU202302600

Initially, in the absence of an external magnetic field, the domains within a material are randomly oriented, resulting in a net magnetization of zero. However, when an external magnetic field is applied, the domains align themselves in parallel with the field direction, causing the material to become magnetized. Interestingly, even after the removal of the magnetic field, some of the material retains a significant level of magnetization. This phenomenon is known as residual magnetization.

The distinction between ferromagnetism and paramagnetism can be observed in the behavior of magnetization under an applied magnetic field. In the case of ferromagnetic materials, as the magnetic field strength increases, the magnetic moments within the material align themselves with the field and eventually reach a point of saturation. At this saturation point, all the magnetic moments are fully aligned, and further increase in the magnetic field does not lead to additional magnetization. In contrast, paramagnetic materials exhibit a continuous increase in magnetization with the applied magnetic field, without reaching a saturation point. The magnetic moments in paramagnetic materials align partially with the field, and their alignment becomes stronger as the field strength increases, but it does not reach full saturation. These distinct magnetization behaviors under magnetic fields allow us to differentiate between ferromagnetic and paramagnetic materials.

Ferromagnetic materials undergo a phase transition and become paramagnetic as the temperature rises above a critical point known as the Curie temperature.

doi:10.6342/NTU202302600

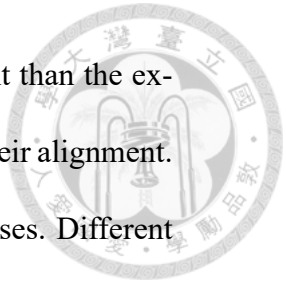

At high temperatures, thermal fluctuations become more significant than the exchange interaction, making it difficult for the domains to maintain their alignment. The material loses its long-range order, and its magnetization decreases. Different ferromagnetic materials exhibit various Curie temperatures, reflecting their unique atomic and magnetic properties.

Antiferromagnetism

Antiferromagnetic materials exhibit a unique magnetic behavior characterized by a net magnetization of zero. In these materials, neighboring magnetic domains align in an antiparallel configuration, resulting in the cancellation of their magnetic moments. The key driving force behind antiferromagnetism is the negative exchange interaction, which causes neighboring spins to align in opposite directions to minimize their total energy.

Due to the antiparallel alignment of spins, antiferromagnetic materials do not possess a macroscopic magnetization, even in the presence of an applied magnetic field. This is in contrast to ferromagnetic materials, where the spins align parallel to each other and produce a nonzero net magnetization.

Similar to ferromagnetic materials, antiferromagnetic materials can also undergo a phase transition at a specific temperature called the Néel temperature. Above this transition temperature, the thermal energy disrupts the antiparallel alignment of spins, and the material becomes paramagnetic. As the temperature decreases below the Néel temperature, the spins start to order again in the antifer-

doi:10.6342/NTU202302600

romagnetic configuration, leading to a restoration of the zero net magnetization.

Ferrimagnetism

Ferrimagnetism is a type of magnetic ordering that exhibits a spontaneous magnetization, similar to ferromagnetism. However, unlike ferromagnetic materials where all magnetic moments align in the same direction, in ferrimagnetic materials, the magnetic moments are aligned in opposite directions but with unequal magnitudes. This unequal alignment leads to a net magnetization, although it is typically smaller than in ferromagnetic materials.

In ferrimagnetic materials, two or more different types of magnetic sublattices coexist. The magnetic moments of these sublattices are aligned in such a way that they do not completely cancel each other out. The unequal alignment results from the difference in the magnetic moments or the exchange interactions between the sublattices. One sublattice typically has a higher magnetic moment than the other, leading to a net magnetization. This net magnetization arises from the incomplete cancellation of the magnetic moments and gives rise to the characteristic mag net properties of ferrimagnetic materials .

Similar to ferromagnetism and antiferromagnetism, ferrimagnetism also undergoes a phase transition at a critical temperature. Above the Curie temperature, thermal energy disrupts the ordered alignment of the magnetic moments, and the material transitions to a disordered, paramagnetic state.

doi:10.6342/NTU202302600

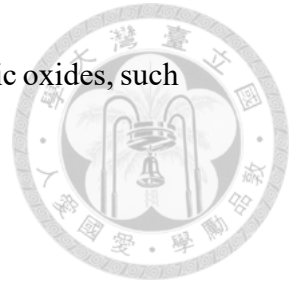

Ferrimagnetic materials are commonly found in various magnetic oxides, such as Fe_3O_4 and $Y_3Fe_5O_{12}$ (YIG, yttrium iron garnet).

Hysteresis Loop

To analyze the behavior of the magnetic moment in materials, the B-H or M-H plot is commonly used to visualize their magnetic properties. For example, in a diamagnetic material, the M-H plot shows a straight line with a negative slope, indicating that the magnetic moment points in the opposite direction of the applied field.

It was mentioned that in ferromagnetic materials, the interaction between neighboring atoms leads to the tendency of retaining magnetization even after the removal of an external magnetic field. The magnetic domain walls, which determine the alignment of magnetic moments, do not return to their original state once the field is removed. This ”memory of magnetic history” is called hysteresis effect.

The hysteresis loop, also known as the B-H loop or M-H loop (as shown in Fig.2.14), graphically represents the relationship between the applied field (H) and the resulting magnetization (M) in ferromagnetic materials. There are several key points and characteristics can be observed in this plot. Saturation field (H_S) is a magnitude of magnetic field that can induce full magnetization in the material. At this point, the material is fully magnetized, and any further increase in the applied field does not result in a significant increase in magnetization. In addition,

doi:10.6342/NTU202302600

saturation magnetization (M_S) is the maximum achievable magnetization in the material when subjected to a sufficiently strong magnetic field. It represents the upper limit of magnetization and is a material-specific property. Moreover, magnetic coercivity (H_C) represents the strength of reverse magnetic field required to demagnetize the material. It is the value of the applied magnetic field where the magnetization reaches zero. It is also a measure of the ability of a ferromagnetic material to withstand an external magnetic field without becoming demagnetized. Nevertheless, after the magnetic field reduce to zero from the saturation field, the material retains a nonzero magnetic flux which indicates the residual magnetization (M_r) in the material.

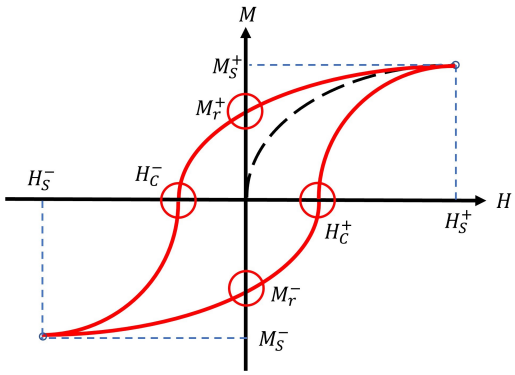

Figure 2.14: Schematic diagram for the hysteresis loop

The hysteresis loop contains information about the magnetization behavior of ferromagnetic materials. Notice that a demagnetized material is initially located at the origin and follows the dashed line in Fig.2.14 as the magnetic field increases.

doi:10.6342/NTU202302600

2.4.2 Anisotropic Magnetoresistance (AMR)

Magnetoresistance (MR) is a phenomena where the electrical resistance of a material changes in response to an applied magnetic field. Anisotropic Magnetoresistance (AMR) is a specific type of magnetoresistance in ferromagnetic metals (FMs) that depends on the angle ϕ between the direction of current flow and the orientation of magnetization, which can be controlled by an external magnetic field.

The origin of AMR can be explained by the scattering anisotropy caused by spin-orbit coupling, which connects the transport properties of conducting electrons to the magnetization in the material. Spin-orbit coupling arises from the interaction between the electron spins and their orbital motion. This gives rise to a various degree of scattering for electrons. Fig.2.15 shows the scattering behavior between electrons and magnetic moments. When the current flows parallel to the direction of magnetization ($\phi = 0$), the electron experience a higher degree of scattering. This leads to a higher resistance, resulting in a maximum value of resistance for this configuration. Conversely, when the current is perpendicular to the magnetization ($\phi = 90$), resulting in a reduced scattering probability and a lower resistance, and thus the resistance reaches its minimum value for this configuration.

doi:10.6342/NTU202302600

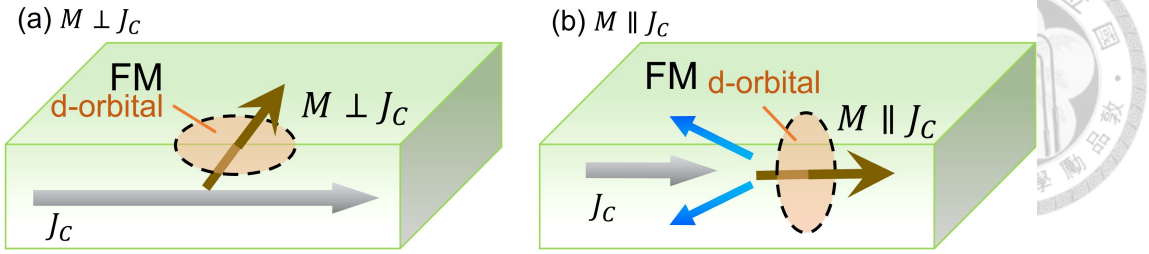

Figure 2.15: Schematic diagram for the AMR. (a) For the case $M \perp J_C$, scattering probability between electron and magnetic moment is less than the (b) $M \parallel J_C$ configuration.

In general, the angle dependence of resistivity ρ_{AMR} can be described as

$$\rho_{AMR}(\phi) = \rho_{\perp} + \left(\rho_{\parallel} - \rho_{\perp}\right) \cos^2 \phi \tag{2.23}$$

where $\rho_{\perp}$ and $\rho_{\parallel}$ represent the resistivity of FM when the magnetization is fully perpendicular and parallel to the current, respectively. Experimental observations of AMR behavior confirm this sinusoidal dependence. Fig.2.16 is the measurement result of angle dependent MR for 10 nm thickness Ni sample. It illustrates the variation in resistance as a function of the angle in each rotation orientation. The β scan, where the magnetic field is always perpendicular to the current, shows a negligible difference in resistance. On the other hand, $alpha$ and $gamma$ scan signal is comparable. Combining these two facts indicating the existence of AMR.

2.4.3 Anomalous Hall Effect (AHE)

The Hall effect is a fundamental phenomena in which a voltage difference, known as the Hall voltage, is generated across a conducting material when a current passes through it in the presence of a perpendicular magnetic field, as Fig.2.17(a). When

doi:10.6342/NTU202302600

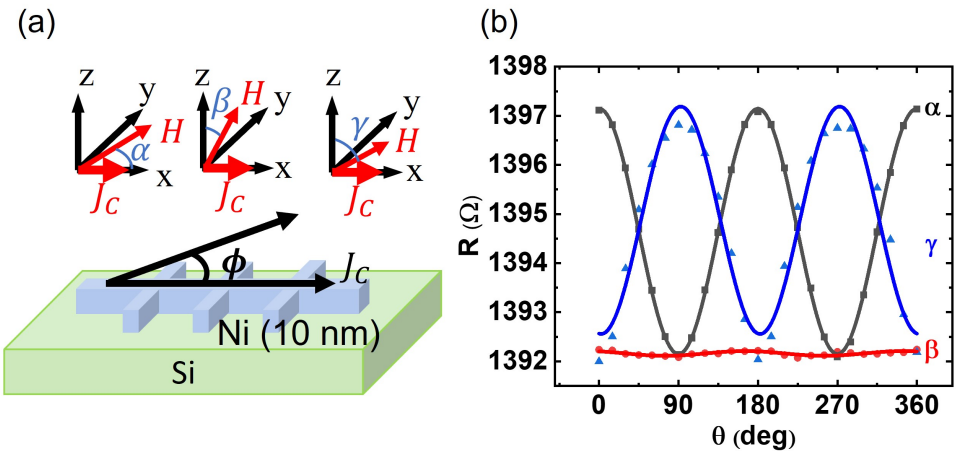

Figure 2.16: (a) Schematic diagram for the MR measurement (b)The angle dependent MR for Ni(10 nm)/Si

a current flows through x-axis in a z-direction external field, electrons experience a force called the Lorentz force, which causes their trajectory to deviate, resulting in an accumulation of charge at the boundary and the generation of a transverse voltage. The Hall voltage depends on the magnitude of current (I), applied field (B), and carrier density (N). By considering the equality of the electric force and the Lorentz force, the Hall resistance is expressed as $\rho_H = \frac{B}{dne} = R_H B$, where R_H is Hall coefficient.

Anomalous Hall Effect (AHE) is a distinct variation of the Hall Effect that occurs in ferromagnetic materials (FMs) (Fig.2.17(b)). Unlike the ordinary Hall Effect, transverse voltage present even in the absence of an applied magnetic field. The anomalous Hall resistance is expressed as

$$\rho_{AHE} = 4\pi R_A M_S \tag{2.24}$$

doi:10.6342/NTU202302600

where M_S is the saturation magnetization of the FM and R_A is the anomalous Hall coefficient.

The origin of AHE can be understood as the result of spin-orbit scattering [26]. Electrons with different spins experience opposite transverse conductivity due to spin-orbit coupling. In FMs, the number of majority-spin and minority-spin electrons are different. As a result, an unequal charge accumulation occurs in the transverse direction, resulting in the emergence of an anomalous Hall voltage difference.

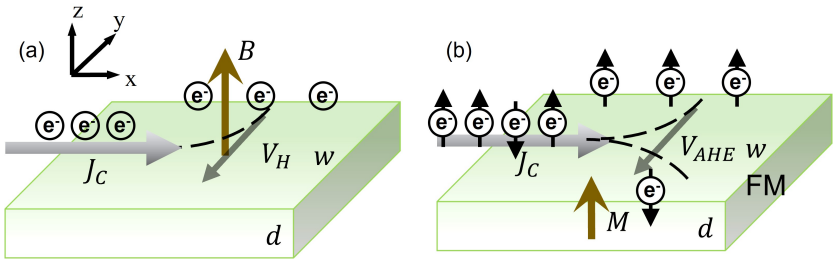

Figure 2.17: Schematic diagram for the (a) OHE and (b) AHE

In FMs, the magnetization can be controlled by external magnetic field. Fig.2.18 shows the field-dependent AHE in a 10 nm thick $Ni_{80}Cu_{20}$ sample on a silicon substrate. At low magnetic field magnitudes, the Hall resistance increases linearly with the magnetic field until it reaches saturation. With further increases in the magnetic field, the Hall resistance remains constant. This demonstrates a strong correlation between the anomalous Hall resistance and the magnetization of the material.

doi:10.6342/NTU202302600

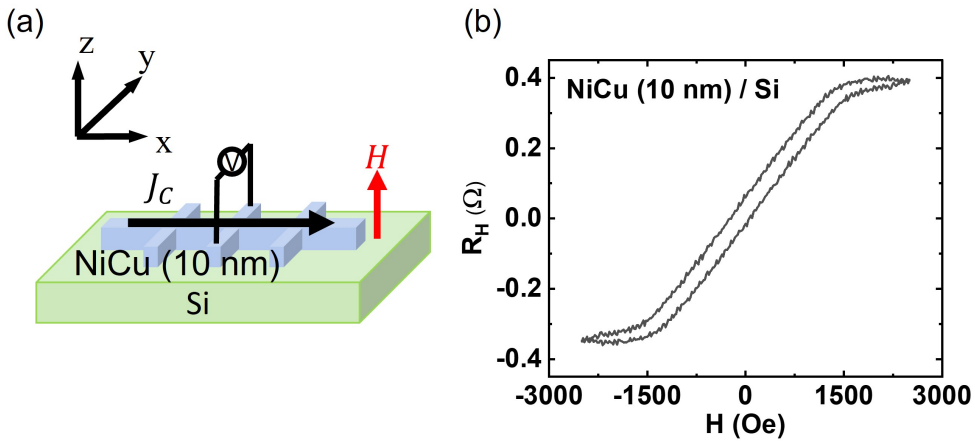

Figure 2.18: The field dependent anomalous Hall resistance for NiCu(10 nm)/Si

2.4.4 Magnetization-Dependent Thermal Voltage

Heat flow in the material cause the same spin or electron response as charge current. An example is that the temperature difference drives the flow of charge, which is known as Seebeck effect (Fig.2.19). When a temperature difference presents between two ends of a metal, an electromotive force (emf) is created. This emf drives the charge accumulate at two ends, resulting an electric field or a voltage difference, which is known as Seebeck voltage. Relation between field and temperature can be described as

$$E_S = -S\nabla T \tag{2.25}$$

where S is Seebeck coefficient. It is an important parameter that determines the performance of thermoelectric effect.

For FMs, the Seebeck coefficient exhibits a similar response to an external magnetic field as AMR. Fig.2.20 shows the field dependent Seebeck voltage in

doi:10.6342/NTU202302600

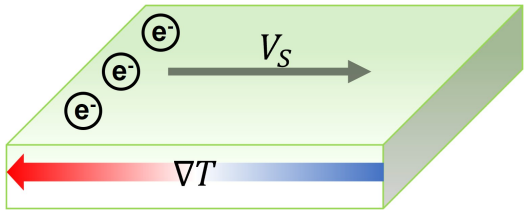

Figure 2.19: Schematic diagram of Seebeck effect

10 nm thick Ni film on a silicon substrate. It has the same behavior with AMR, except upside down. The saturation in large field indicate a correlation between the voltage difference and the magnetization. Consequently, this effect is specific to FMs.

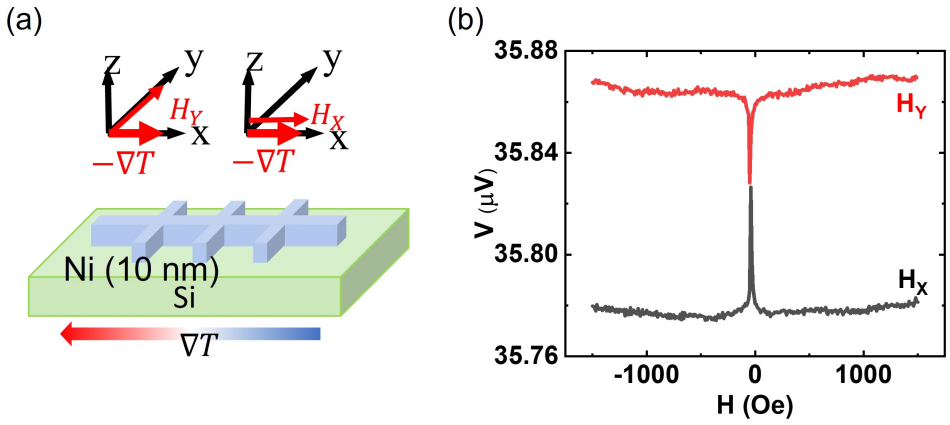

Figure 2.20: (a) Schematic diagram for the thermal voltage measurement (b)The field dependent magnetization-dependent thermal voltage for Ni(10 nm)/Si

2.4.5 Anomalous Nernst Effect (ANE)

Thermoelectric effect has similar phenomena corresponding to Hall effect, which is called Nernst effect. Fig.2.21(a) shows the schematic diagram of ordinary Nernst effect. When a temperature gradient and magnetic field are applied along

doi:10.6342/NTU202302600

x- and y-axis, an electric field or a voltage difference is induced in the z-direction.

For FMs, anomalous Nernst effect (ANE) leads to a transverse voltage difference under a temperature gradient even in the absence of a magnetic field. This effect can be describe as

$$E_{ANE} = -S_{xy} m \times \nabla T \tag{2.26}$$

where E_{ANE} is electric field induced by ANE, S_{xy} is anomalous Nernst coefficient, and m is the direction of the magnetic moment.

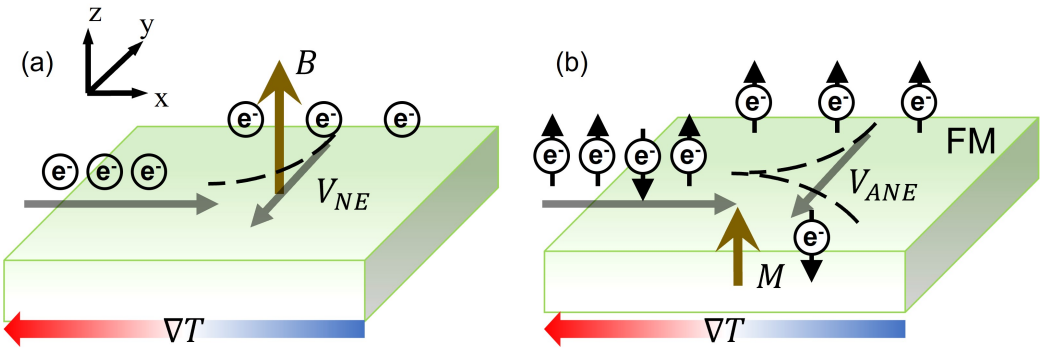

Figure 2.21: Schematic diagram of (a) ONE and (b) ANE

doi:10.6342/NTU202302600

Chapter 3 Method

In the previous chapter, we discuss the fundamental concepts of spintronics and magnetism, laying the foundation for our study on the spin Nernst effect in the ferromagnetic state of the $Ni_{80}Cu_{20}$ alloy. In this chapter, we introduce how the samples are prepared and the measurement techniques employed.

Our experimental setup involves depositing Pt, Ni, and $Ni_{80}Cu_{20}$ layers in the form of a Hall bar pattern onto substrates using a magnetron sputtering system. To ensure accurate deposition, the sputtering rate is determined by measuring the thickness of samples deposited for different duration. The thickness is identified using X-ray reflection (XRR) technique. The Hall bar pattern is accomplished through the photo-lithography. However, before this step, it is essential to carry out a cleaning process for the substrates to ensure pattern and film quality.

Once the samples are prepared, we proceed to measure their physical properties. Firstly, it is crucial to confirm the element ratio, particularly the $Ni_{80}Cu_{20}$ composition. X-ray Diffraction (XRD) analysis is employed to identify the location of characteristic peaks, which indicatea a near 80:20 ratio of the constituent elements. To assess the magnetic properties of the samples, vibrating sample magnetometer (VSM) is utilized to obtain the magnetization versus magnetic field (M-H) plot. This allows us to examine the behavior of magnetization under varying

doi:10.6342/NTU202302600

magnetic field conditions. Finally, we conduct an electric and a thermoelectric measurements under an applied magnetic field. These measurements aim to explore the relationship between electrical and thermoelectric properties and the external magnetic field.

3.1 Sample Preparation

3.1.1 Substrate Cleaning

The cleaning treatment of the substrate is essential steps in the sample preparation process to ensure the removal of any oil stains and dust particles that could affect the experimental results. This is crucial to achieve a clean and pristine surface for subsequent deposition and measurements.

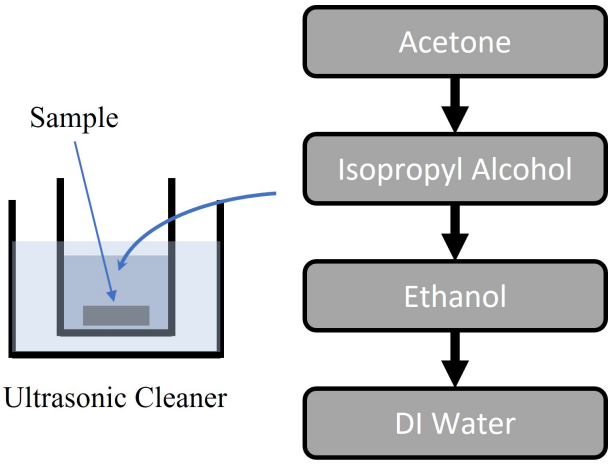

Figure 3.1: Flow chart of substrate cleaning

The cleaning procedure involves several solvents, as shown in Fig.3.1. The substrate is first immersed in acetone, then isopropyl alcohol (IPA) to dissolving

doi:10.6342/NTU202302600

organic contaminants. Ethanol further removes any remaining contaminants on the substrate surface. Finally, DI water eliminates the residual organic solvents. The cleaning process takes place in an ultrasonic cleaner, which provides enhanced cleaning efficiency by generating high-frequency sound waves.

3.1.2 Photo-lithography

Photo-lithography is a crucial technique employed in the fabrication of microstructures and patterns on a substrate. It involves a series of steps that utilize light-sensitive materials called photoresists to transfer a desired pattern onto the substrate surface.

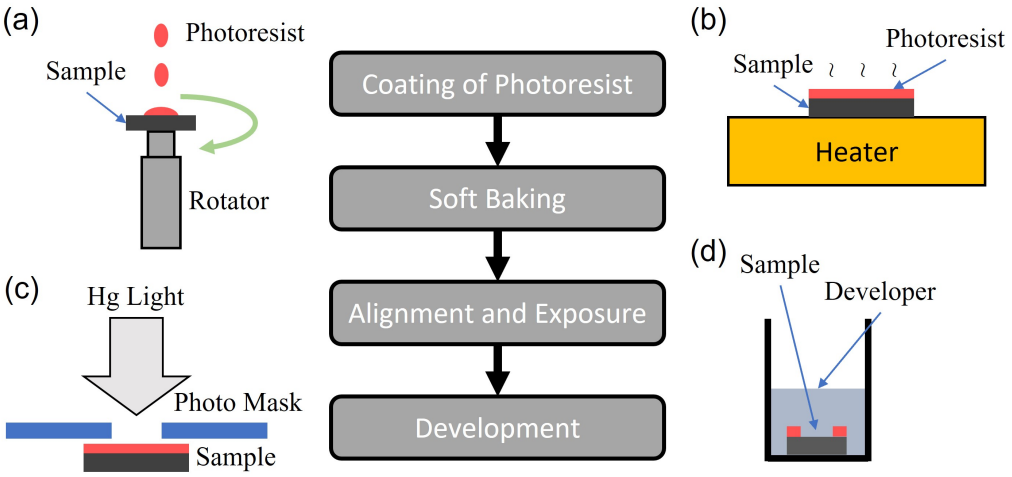

Figure 3.2: Flow chart of photo-lithography. (a) Coating of Photoresist (b) Soft Baking (c) Alignment and Exposure (d) Development

The photo-lithography process typically consists of the following steps:

1. Coating of photoresist: A thin layer of photoresist is spin-coated onto the

doi:10.6342/NTU202302600

substrate surface. The photoresist is a light-sensitive material that undergoes chemical changes upon exposure to light, allowing for the transfer of the desired pattern.

2. Soft baking: After the photoresist is coated, the substrate is subjected to a gentle heating process known as soft baking. This makes the chemical structure of photoresist become stronger.

3. Alignment and exposure: The substrate is aligned in an exposure system, where a mask containing the desired pattern is placed in close proximity. The photoresist-coated substrate is then exposed to a light source. In our experiment, we use Hg light. The pattern on the mask is transferred to the photoresist.

4. Development: Following exposure, immerse the substrate in a developing solution that selectively removes either the exposed or unexposed regions of the photoresist, depending on whether a positive or negative resist is used. This step reveals the desired pattern on the substrate surface.

The process differs significantly depending on whether we use positive or negative photoresist. In the case of positive photoresist, the residual photoresist covers the areas where we do not want the film. We begin with a clean substrate without any film, apply the photolithography process, and then deposit the desired film. Afterward, the sample is immersed in an organic solution to wash out the photoresist, a technique known as lift-off. The film directly deposited on the substrate

doi:10.6342/NTU202302600

remains on the sample, while the photoresist and any film deposited on top of it are removed, resulting in the desired pattern.

Conversely, with negative photoresist, the residual photoresist covers the areas where we want to keep the film. In this case, the film is deposited first. Subsequently, during the photolithography process, the areas of the film not covered by the photoresist are targeted for removal, which is achieved through a technique called etching. There are several methods available for etching, such as wet etching or plasma etching.

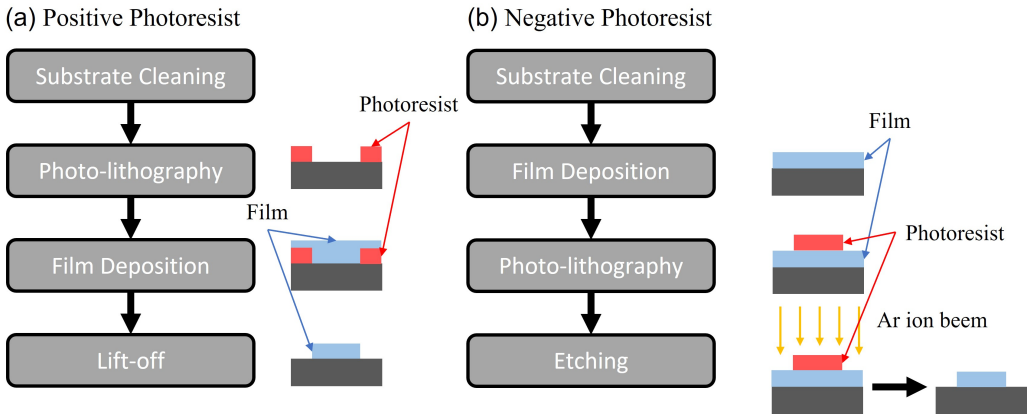

Figure 3.3: Flow chart of sample preparing for positive and negative photoresist. (a) Positive Photoresist (b) Negative Photoresist

doi:10.6342/NTU202302600

3.1.3 Magnetron Sputtering Deposition

Sputtering deposition is a widely used physical vapor deposition (PVD) technique that offers several advantages over other deposition methods such as pulsed laser deposition (PLD) and thermal evaporation. It allows for the rapid fabrication of films with excellent uniformity and is applicable to a wide range of materials, including metals, semi-metals, and insulators.

The setup of a magnetron sputtering system involves an anode and a cathode. The sample to be coated is placed at the anode, while the target material, which is the desired deposition material, is positioned at the cathode.

The process of sputtering involves creating an environment of electrically neutral argon (Ar) gas. Argon gas is chosen for two main reasons. Firstly, it is an inert gas that prevents chemical reactions during the deposition process. Secondly, argon is easily ionized.

In a high vacuum environment, Ar atom is easily ionized. This produces positively charged Ar ions and negatively charged electrons. Under a strong electric field, the Ar ions are accelerated towards the cathode, bombarding the target surface with high energy Fig.3.4(c). As a result, atoms from the target are ejected and finally condense onto the substrate, forming a thin film. Simultaneously, the electrons released from the ionized Ar atoms also experience acceleration and collide with residual argon atoms, leading to further ionization and the generation of

doi:10.6342/NTU202302600

more Ar ions and free electrons.

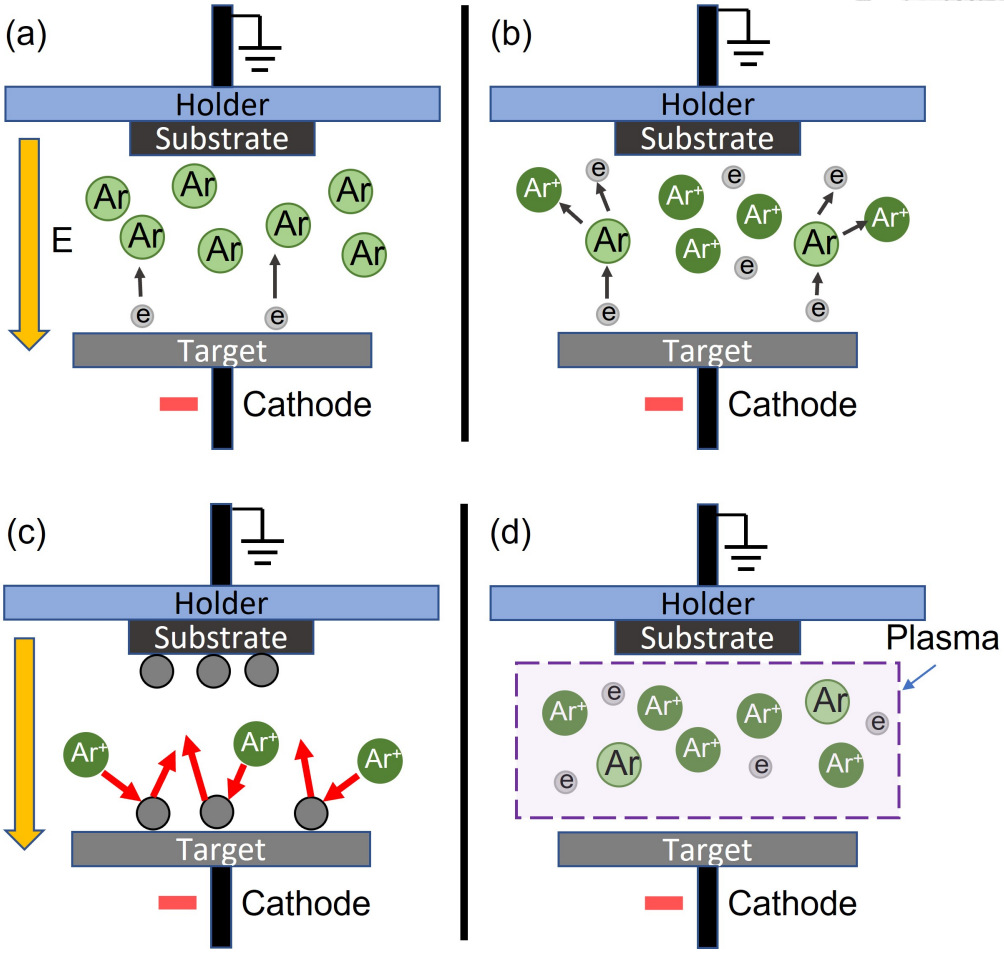

Figure 3.4: Schematic diagram of the basic sputtering process.

Magnetron sputtering is a technique commonly employed to enhance the efficiency of sputtering, particularly for magnetic materials. By utilizing a magnet, a strong magnetic field is created, trapping electrons in a confined region near the target. This magnetic confinement offers several benefits, including increased deposition efficiency, protection of the film from plasma damage, and the ability to achieve larger areas of uniform thin film deposition.

doi:10.6342/NTU202302600

3.1.4 X-ray Reflection (XRR)

The sample we measure is a film on a substrate. The film is made by sputtering deposition. Before practicing this technique, the sputtering rate, the sputtering thickness in a unit time under a fixed condition, needs to be confirmed first.

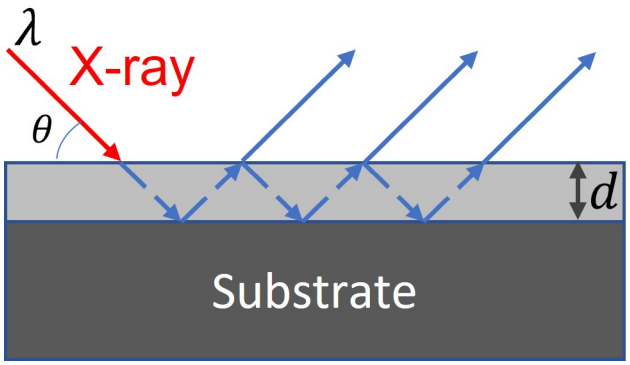

Figure 3.5: Schematic diagram for thickness measurement using X-ray reflectivity (XRR).

There are many means to confirm the thickness of films, such as atomic force microscopy (AFM), surface profiler (α-step). In this work, X-ray reflectivity (XRR) is used to measure the thickness of thin films. For a low roughness and negligible refraction effect sample, the relation between thickness and x-ray incidence angle obeys Bragg equation

$$m\lambda = 2d\sin\theta_m, \quad m \in N \tag{3.1}$$

where m is any positive integer, λ is the wavelength of incident X-rays, d is thickness of the film, and θ_m is the angle between incident X-rays and sample surface, as shown in Fig.3.5. Fig.3.6 shows an example of XRR result with a Pt film. The

doi:10.6342/NTU202302600

thickness is obtained by adapting eq.3.1 with the position of each peak.

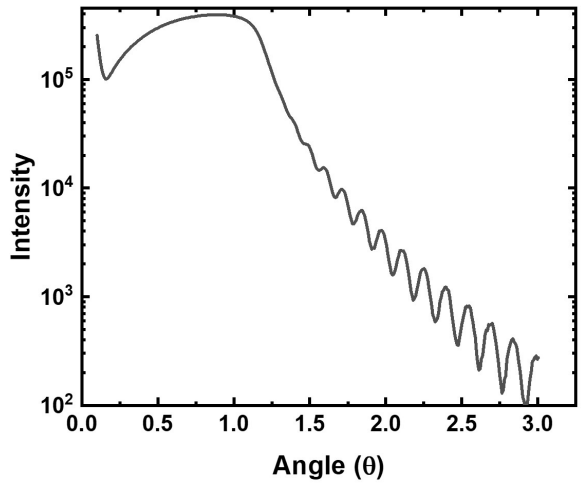

Figure 3.6: An example of XRR result.

3.2 Physical Properties Measurement

3.2.1 X-ray Diffraction (XRD)

X-ray diffraction (XRD) is a technique used to analyze the crystal structure of materials by scanning X-rays at different angle. As shown in Fig.[], when incident X-rays interact with the atomic layers of a crystalline material, diffraction occurs. However, only X-rays with a specific angle of incidence, denoted as θ, that satisfies the condition of the X-ray's travel distance being equal to an integer multiple of the X-ray wavelength, will produce constructive interference, resulting in distinct peaks of intensity in the diffraction pattern. The position of these peaks follows Bragg's Law (eq.3.1), where d in this case denotes the spacing between atomic

doi:10.6342/NTU202302600

layers.

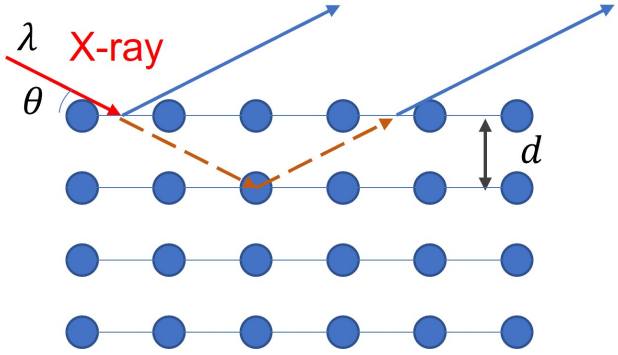

Figure 3.7: Schematic diagram for crystal structure measurement using X-ray diffraction (XRD).

It has been reported that the composition of NixCu$_1$−x alloy is estimated through the position of characteristic peak. Since nickel (Ni) and copper (Cu) have the same crystal structure of face center cubic (space group: $Fm\bar{3}m$), the alloy also has the same crystal structure. The lattice constant depend on the ratio of their composition. In [12], the linear relation between the position of characteristic peak and the content of Ni is demonstrated. Thus in our experiment, we can utilize this technique to measure the composition of the Ni-Cu alloy. By analyzing the position of the alloy peaks in the X-ray diffraction pattern, we can obtain valuable information about the relative amounts of Ni and Cu present in the alloy.

3.2.2 Vibrating Sample Magnetmeter (VSM)

Magnetic property measurement is an essential characterization technique used to investigate the magnetic behavior of materials. One commonly employed instru-

doi:10.6342/NTU202302600

ment for this purpose is the Vibrating Sample Magnetometer (VSM). The VSM is used to measure the magnetic moment of a sample as a function of an applied magnetic field. It provides valuable information about the sample's magnetic properties, such as M-H loop.

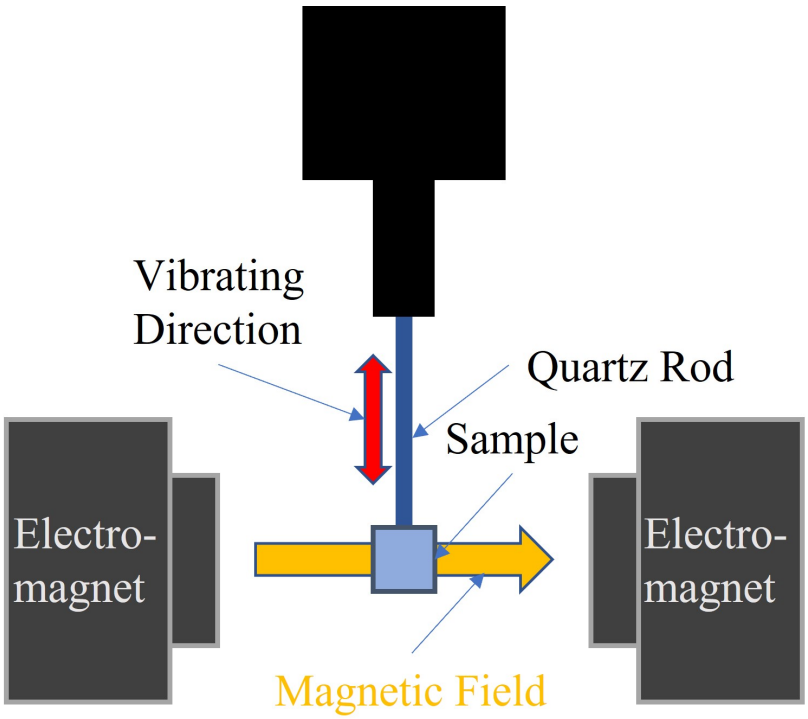

Figure 3.8: Schematic diagram for the Vibrating Sample Magnetometer measurement

The measurement process in a VSM involves placing the sample under a magnetic field generated by an electromagnet. The sample is typically set on the end of a quartz rod, and the other end is fixed on the vibrator.

The VSM measures the magnetic moment of the sample by detecting the induced voltage resulting from the vibration of the sample. When the sample is placed in the uniform magnetic field, the material is magnetized. Subsequently,

doi:10.6342/NTU202302600

the total magnetic field is contributed by the external field and the stray field induced by magnetization in the magnetic material. However, this additional field is far less than the external field, a more sensitive measuring method should be exploit. Oscillating the sample induces an alternating electric field in the detecting coil based on Faraday's Law. This field is proportional to the magnetic moment. By means of extracting the vibrating frequency signal with lock-in amplifier, we can obtain the field dependent magnetization plot, known as M-H plot. This plot provides information about the sample's magnetic response, including its saturation magnetization, residual magnetization, and coercivity.

3.2.3 Electrical Four-point Probe Measurement

In this study, we employed the four-point probe technique to measure the resistivity of the sample. This technique is particularly advantageous as it helps mitigate the contribution of contact resistance, leading to accurate and reliable measurements.

The two-point probe measurement method utilizes only two probes for both current injection and voltage measurement. However, this approach is prone to errors caused by additional resistance introduced by the contact points. Fig. 3.9(a) illustrates that the voltage measurement includes the voltage drop across the contact resistances themselves. Consequently, for samples with very low resistance, the two-point probe measurement method introduces significant errors.

On the other hand, the four-point probe measurement technique (Fig. 3.9(b))

doi:10.6342/NTU202302600

utilizes two additional probes for voltage measurement while passing a known current through the sample. Although this introduces more contact points, the high-impedance nature of the voltmeter ensures that current does not flow through these contacts. As a result, additional voltage drops are avoided, leading to more precise measurements.

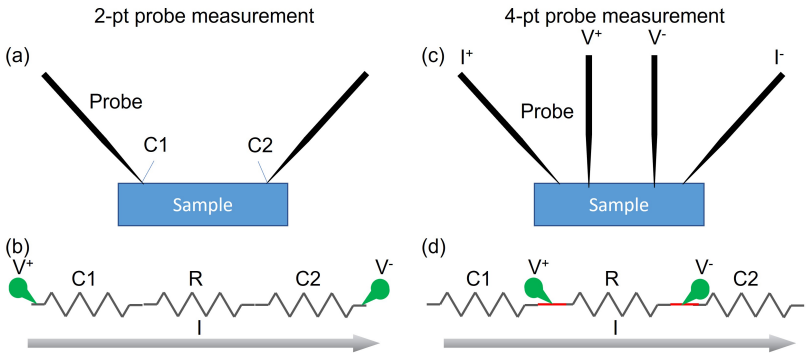

Figure 3.9: Schematic diagram for (a) 2-pt and (c) 4-pt measurement. Effective resistance in (b) 2-pt and (d) 4-pt measurement. The C1 and C2 represent the contact resistance between probes and the sample.

The four-point probe technique finds applications in magnetoresistance (MR) measurements, where the resistance of a material varies under an applied magnetic field. It is worth noting that for the material in our experiment, the resistance difference in MR measurements is about four orders of magnitude smaller than the sample resistance itself. Therefore, achieving an accurate measurement of resistivity is crucial for obtaining reliable MR data.

doi:10.6342/NTU202302600

3.2.4 Thermoelectric Measurement

For the thermal measurements, we employed two different temperature gradient directions in our experiment: out-of-plane and in-plane temperature gradients, which allowed us to investigate the spin Seebeck effect and the spin Nernst-induced thermal power, respectively.

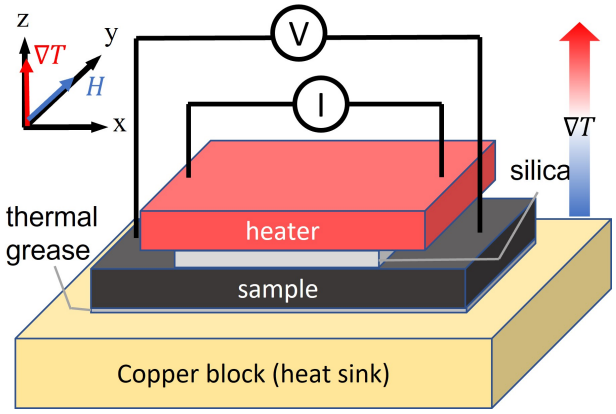

Figure 3.10: Schematic diagram for thermal measurement with out-of-plane temperature gradient

In the case of the out-of-plane temperature gradient measurement, the experimental setup is illustrated in Fig.3.10. To generate the out-of-plane temperature gradient, we position the sample between an SMD resistor acting as a heat source and a copper block functioning as a heat sink. The SMD resistor, characterized by its small size and square shape, provides convenient contact. When a current is applied to the resistor, Joule heat is generated and flows through the sample, dissipating into the copper block. To enhance the contact and thermal conduction, a silica pad is placed between the heater and the sample, while thermal grease with

doi:10.6342/NTU202302600

high thermal conductivity is applied between the sample and the copper block. The temperature difference between the top and bottom of the sample can be measured using a thermocouple. In order to perform thermal spin transport measurements, an external magnetic field is applied, and the resulting voltage response is detected by a voltmeter.

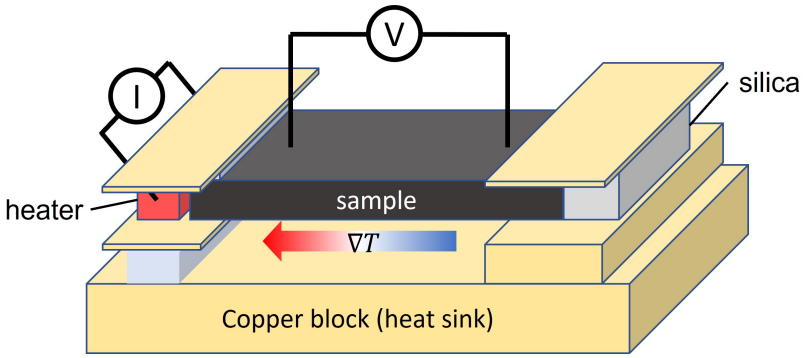

Figure 3.11: Schematic diagram for thermoelectric measurement with in-plane temperature gradient

On the other hand, for the in-plane temperature gradient measurement, the experimental setup is depicted in Fig.3.11. Similarly, the SMD resistor acts as the heat source. The sample is positioned between the heat source terminal, which is separated from the copper block, and the heat sink terminal, which directly contacts the copper block. When a current is applied to the resistor, Joule heat is generated, propagating through the sample and dissipating into the copper block. To establish contact between the sample and the two terminals, two copper clips are used to facilitate heat transfer from the heater to the sample and from the sample to the heat sink. The temperature difference across the sample and the magnetic field-dependent thermal voltage are detected using a thermocouple and a

doi:10.6342/NTU202302600

voltmeter, respectively.

doi:10.6342/NTU202302600

Chapter 4 Result and Discussion

4.1 Introduction

In this chapter, we explore the presence of spin Hall magnetoresistance (SMR) in a $Ni_{80}Cu_{20}$/YIG sample by comparing it to different control samples. The control samples include Ni/Si, which exhibits only anisotropic magnetoresistance (AMR) without SMR, and Pt/YIG, which displays only SMR without AMR. Furthermore, we find that the spin Hall angle obtained from SMR is consistent with the angle obtained from spin Seebeck effect (SSE) measurements. Additionally, we measure the spin Nernst effect-induced thermal power in $Ni_{80}Cu_{20}$/YIG and compare it with the Pt/YIG control sample.

In this study, the prepared sample consists of $Ni_{80}Cu_{20}$, Pt, and Ni thin films which is deposited on YIG and Si substrates using magnetron sputtering technique. The film is lifted off into a Hall bar pattern by a photo-lithography process. The crystal structure and elemental composition are characterized using XRD measurements with Cu $K\alpha$ radiation (λ=0.154 nm), as depicted in Fig.4.1 (a). By comparing the characteristic peak with Fig.4.1 (b), the element ratio of Ni and Cu is confirmed to be 80:20. The magnetic properties are measured using a VSM, as shown in Fig.4.2, confirming the $Ni_{80}Cu_{20}$ film with 10 nm thickness is in FM

doi:10.6342/NTU202302600

state. The saturation field (H_S) in out-of-plane direction is approximately 1700 Oe. Therefore, applying a 3000 Oe magnetic field during measurements ensures the alignment of all magnetic moments in $Ni_{80}Cu_{20}$.

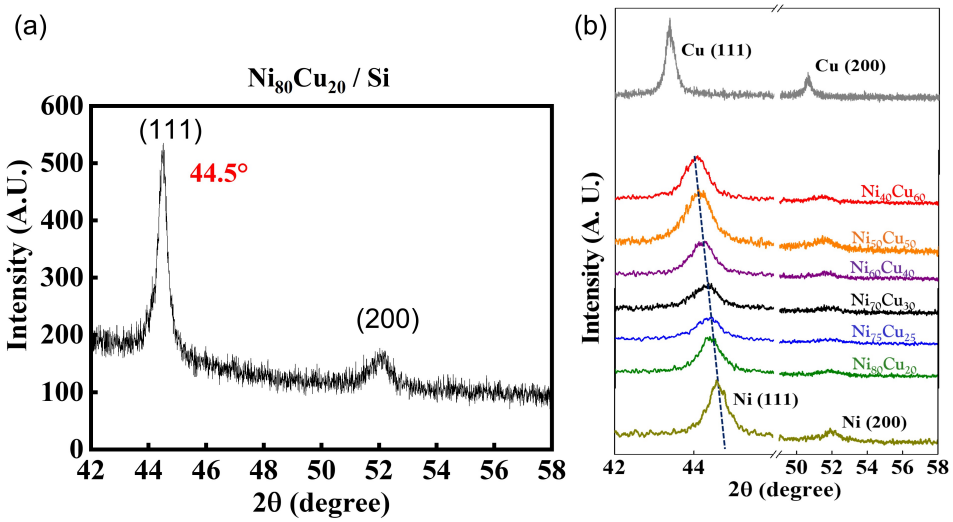

Figure 4.1: (a) X-ray diffraction pattern for the thickness of 500 nm $Ni_{80}Cu_{20}$. (b) X-ray diffraction pattern in different composition of $Ni_{80}Cu_{20}$ [12]

4.2 Spin Hall Magnetoresistance

We have discussed the distinct mechanisms of AMR and SMR. To practically compare these properties, we utilize Ni/Si and Pt/YIG as control groups to investigate the characteristics of these two signals under different directions of the magnetic field. We present the results for the ferromagnetic (FM) state of NiCu/YIG and compare them with the control groups to identify the MR ratio attributed to SMR. By analyzing these results, we determine the spin Hall angle.

doi:10.6342/NTU202302600

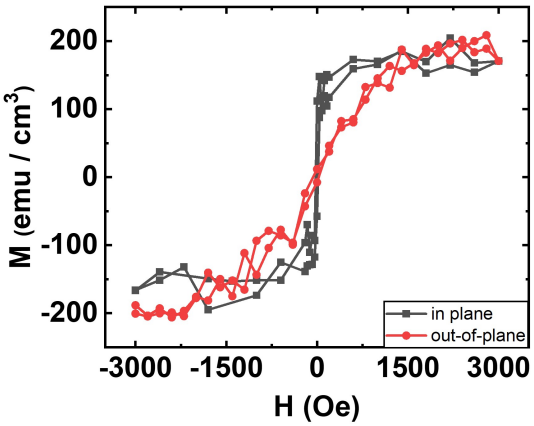

Figure 4.2: The M-H curve for the thickness of 10 nm $Ni_{80}Cu_{20}$ film on Si substrate under in-plane and out-of-plane magnetic field.

4.2.1 Ni/Si

The field-dependent MR behavior of the 10 nm thick Ni film is illustrated in Fig.4.3. The resistance under a magnetic field in the x and y directions is depicted by the black and red curves, respectively. These curves exhibit identical resistance values at zero fields and saturate at approximately 300 Oe. In contrast, magnetic anisotropy emerges in the z direction, which is represented by blue curve, reaching saturation at around 4500 Oe. Once the magnetic moment reaches saturation, the resistance value remains fixed. To compare the differences in resistance for each field direction, we specifically examine the values obtained at high magnetic fields.

As mentioned in the previous chapter, the origin of the resistance difference is related to the orbital plane and the direction of the magnetic moment. Notably,

doi:10.6342/NTU202302600

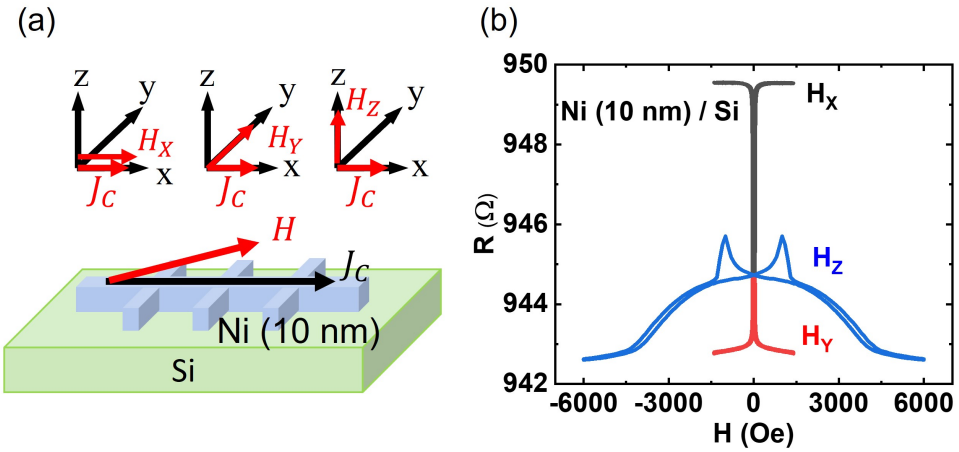

Figure 4.3: Field dependence Magnetoresistance for Ni/Si. (a) Schematic diagram for MR measurement in field scan method. (b) MR measurement result for Ni (10 nm)/Si. The black, red, and blue curves represent the resistance under magnetic field along x, y, and z direction. The teeth feature in blue curve may origin from miss alignment.

the resistance exhibits a significant difference when the magnetic field is applied along the $x-$ and $z-$axis, indicating a lower scattering rate between electrons and orbitals in the z direction compared to the x direction due to the cross-sectional nature of the orbitals. Conversely, the resistance difference is negligible when the magnetic field is applied along the y and z directions. This observation suggests that the scattering rate between electrons and orbitals is equally low in both directions. The MR characteristics in Ni precisely consist with the angle dependent result (Fig.2.16) and match those descriptions in AMR.

doi:10.6342/NTU202302600

4.2.2 Pt/YIG

Unlike Ni, Pt is not an magnetic material thus the magnetic field do not affect the resistance of Pt itself. However, the applied field affect the resistance of Pt/YIG bilayer. The MR behavior with magnetic field scan for Pt/YIG sample is shown in Fig.4.4. The resistance has equal value in zero field, vary with field significantly under low field, and saturate in large field during the field scanning. The behavior of signal saturation under a specific magnetic field is the same as that of magnetic materials, thus we attribute this signal to the additional YIG layer.

Recall that under large field, most of magnetic moment in YIG align to the field. In addition, the resistance is larger when the field is along to x direction than that to y. This indicates that resistance depend on whether the direction of spin and magnetic moment are parallel or perpendicular. On the other hand, under low field, magnetic moments are disordered, thus each curve contact. In addition, magnetic anisotropy also emerges in YIG under the z direction field, which is represented by blue curve, reaching saturation at around 1700 Oe. Moreover, the plateau behavior in y direction origin from non-collinear magnetization between surface and bulk, as mention in [27].

As mentioned in the previous chapter and referenced from [23], Pt/YIG exhibits a significant beta scan signal and no gamma scan signal, which is in contrast to the AMR behavior observed in Ni. This MR behavior observed in the Pt/YIG bilayer is consistent with the results shown in Fig.4.4 and corresponds to the de-

doi:10.6342/NTU202302600

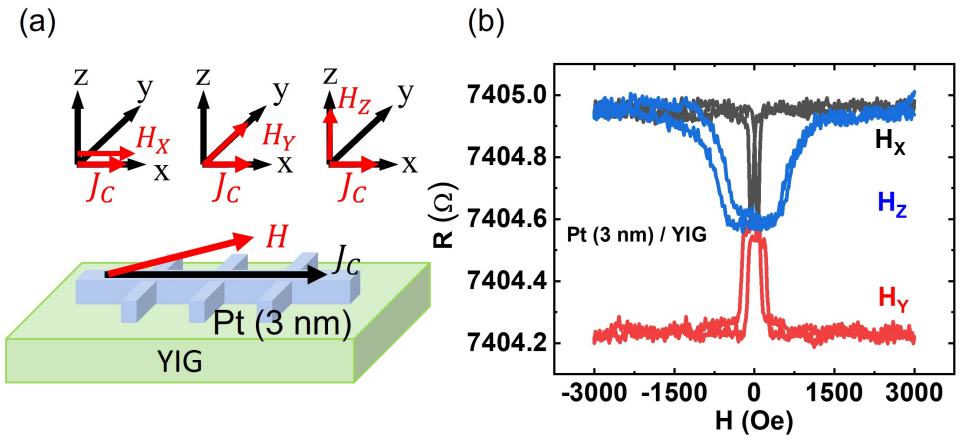

Figure 4.4: Field dependence Magnetoresistance for Pt/YIG. (a) Schematic diagram for MR measurement in field scan method. (b) MR measurement result for Pt (3 nm)/YIG. The black, red, and blue curves represent the resistance under magnetic field along x, y, and z direction.

scriptions of SMR.

By the SMR contribution of MR ratio, the spin Hall angle is estimated by eq.2.12. The MR ratio for Pt/YIG in Fig.4.4 is

$$\frac{\Delta R_{XX}}{R^Z_{XX}} = \frac{R^Y_{XX} - R^Z_{XX}}{R^Z_{XX}} = 9.5 \times 10^{-5} \tag{4.1}$$

Choosing spin diffusion length $\lambda_S = 1.5$ nm, spin mixing conductance $G_{\uparrow\downarrow} = 4 \times 10^{14}\ \Omega^{-1} cm^{-2}$ [28], we obtain the value of spin Hall angle $\pm 1.8\%$. As a heavy metal with strong spin-orbit coupling, Pt is demonstrated for the high efficiency of charge-to-spin conversion.

By comparing the Ni/Si and Pt/YIG result, we conclude that the difference in resistance under an applied magnetic field in the x and z directions signifies AMR

doi:10.6342/NTU202302600

in magnetic materials, while the difference in resistance in the z and y directions represents SMR in certain material/YIG bilayers. Therefore, when measuring the spin Hall angle for other materials, we can focus on the beta scan in angle dependent or y, z direction in field dependent MR measurement.

4.2.3 NiCu/YIG

Based on the method above, SMR and spin Hall angle for $Ni_{80}Cu_{20}$/YIG bilayer can easily be measured. The only difference is that the NiCu is in ferromagnetic state, which may exist magnetic phenomena. Fig.4.5 shows the angle dependent MR with applied field in 3000 Oe, which is large enough to saturate the magnetic moment in 10 nm thick $Ni_{80}Cu_{20}$ known from VSM result (Fig.4.2). There are MR signals in both beta and gamma scan, indicated the contribution of AMR and SMR by comparing Ni and Pt/YIG measurement result.

We focus on SMR contribution of the signal, which has MR ratio

$$\frac{\Delta R_{XX}}{R^{Z}_{XX}} = 6.02 \times 10^{-4}. \tag{4.2}$$

According to the ref.[12], we choose spin diffusion length $\lambda_S = 0.42$ nm, spin mixing conductance $G_{\uparrow\downarrow} = 6.2 \times 10^{13}\ \Omega^{-1}cm^{-2}$, obtaining the spin Hall angle $\pm 12\%$. Comparing with Pt/YIG result, we demonstrate the high efficiency of charge-to-spin conversion comparable to heavy metal. This result proves that ferromagnetic $Ni_{80}Cu_{20}$ also exist strong SOC.

An unexpected result present in field scan which shown in Fig.4.6. The differ-

doi:10.6342/NTU202302600

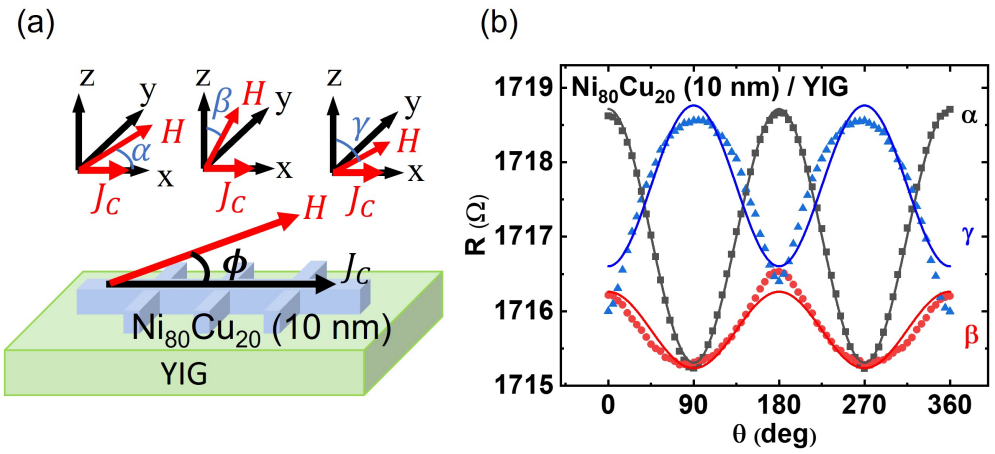

Figure 4.5: Angle dependence Magnetoresistance for NiCu/YIG. (a) Schematic diagram for MR measurement in angle scan method. (b) MR measurement result for $Ni_{80}Cu_{20}$ (10 nm)/YIG. The black, red, and blue curves represent the α scan, which scans in xy plane, β scan, which scans in yz plane, and γ scan, which scans in xz plane, respectively.

ence of resistance with field along x and z direction shows the existence of AMR from NiCu itself, and along y and z direction indicates the spin current generated by SHE from $Ni_{80}Cu_{20}$.

However, each of the signal exist a significant negative MR which grow larger as the magnetic field continuous increases. This might not attribute to non-saturation of magnetic moment due to the range of scan field is out of saturation field in $Ni_{80}Cu_{20}$ and YIG. In addition, there is an obviously transition point in z-direction curve at about 1500 Oe. By comparing with VSM result in Fig.4.2, the magnetic moment is assumed to be saturated when the applied field is larger then 1500 Oe. Moreover, the slope of resistance and field fixed in large field, which may keep the MR ratio invariant. This feature makes the angle scan result reliable.

doi:10.6342/NTU202302600

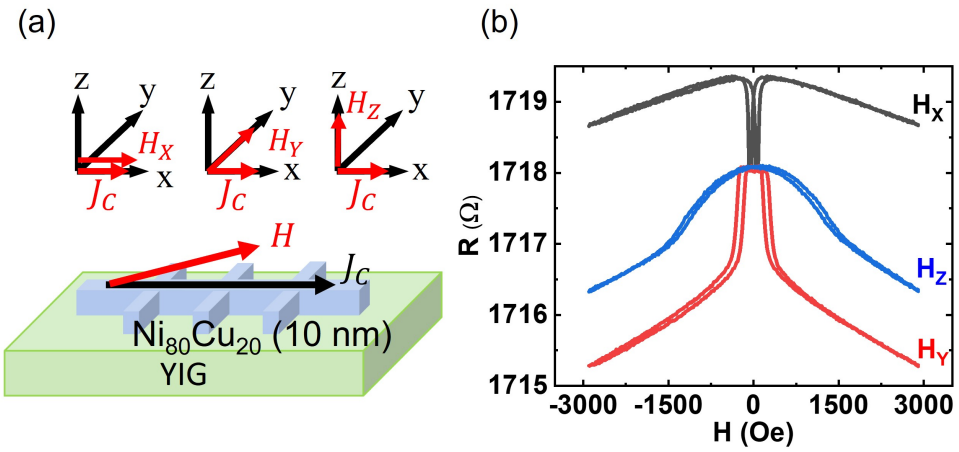

Figure 4.6: Field dependence Magnetoresistance for NiCu/YIG. (a) Schematic diagram for MR measurement in field scan method. (b) MR measurement result for $Ni_{80}Cu_{20}$ (10 nm)/YIG. The black, red, and blue curves represent the resistance under magnetic field along x, y, and z direction.

4.3 Spin Seebeck Effect Measurement

Beside the SMR, which directly observe both charge-to-spin and spin-to-charge conversion, SSE measurement, though indirectly observed by only inverse spin Hall effect, also provides a way to obtain the spin Hall angle in a material. We take YIG as spin current generator and $Ni_{80}Cu_{20}$ as detector. By measuring the voltage between two ends of $Ni_{80}Cu_{20}$, the ISHE signal is obtained, and the spin Hall angle is further calculated. We expect the value is consistent with the result from SMR measurement and the previous research [12].

doi:10.6342/NTU202302600

4.3.1 NiCu/YIG

The red curve in Fig.4.7(b) shows the SSE measurement result for NiCu 10 nm on YIG. The voltage is measured along x-axis, the out-of-plane temperature gradient in 17 K/mm is applied along z-axis, and the in-plane magnetic field is applied along y-axis. The anti-symmetric loop indicate the signal depend on the magnetic moment, and the plateau behavior in low field origin from non-collinear magnetization between surface and bulk, as mention in [27].

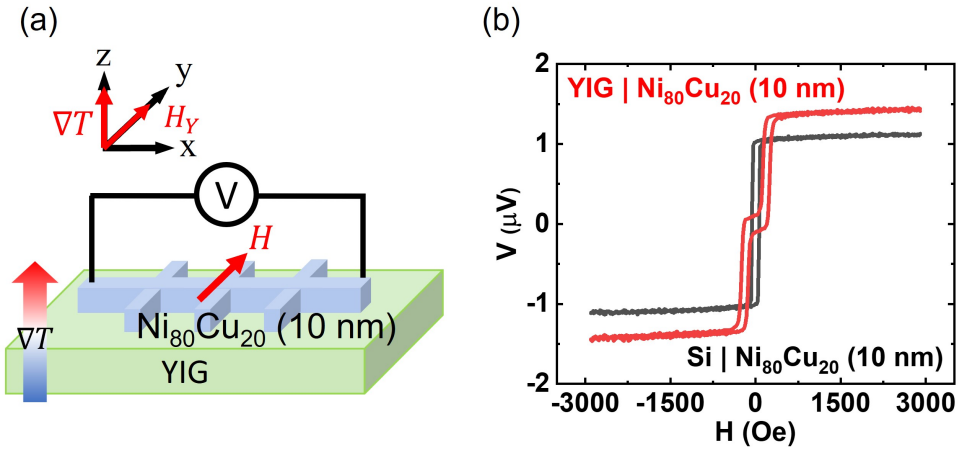

Figure 4.7: (a) Schematic diagram for out-of-plane temperature gradient thermoelectric measurement (b) Field dependence SSE in NiCu/YIG(red curve) and ANE in NiCu/Si(black curve)

However this signal isn't totally attributed to SSE in YIG and ISHE in NiCu. In contrast, ANE in $Ni_{80}Cu_{20}$ provide a large signal. The ANE voltage for NiCu/Si is shown as the black curve in the same figure which has the same measurement structure as $Ni_{80}Cu_{20}$/YIG. The non-zero signal of hysteresis curve implies that

doi:10.6342/NTU202302600

NiCu contribute a part of signal which should be subtracted. By subtracting directly, we get the ISHE voltage

$$V_{ISHE} = V - V_{ANE} = V_{YIG} - V_{Si} \tag{4.3}$$

Same as SMR, we choose spin diffusion length $\lambda_S = 0.42$ nm, spin mixing conductance $G_{\uparrow\downarrow} = 6.2 \times 10^{13}\ \Omega^{-1}cm^{-2}$. Then we have the spin Hall angle 13.7%. This result is consistent to the result from SMR with additional information of sign, which is essential for later experiment.

Material	Thermal Conductivity ($W/m \cdot K$)
Si	380 [29]
YIG	8.2 [30]

Table 4.1: Thermal conductivity for Si and YIG substrates.

In most situations, it is not recommended to subtract two signals directly from two samples, especially when the substrates have different thermal conductivity as indicated in Table 4.1. Moreover, the temperature gradient in the NiCu layer also varies, which leads to distinct signal values. However, in our current setup, we have met sufficient conditions to perform this operation. Firstly, the heat capacity of the heat sink is large enough to assume that its temperature will not change. Secondly, the sample size is the same, including width, length, distance between two probes, and thickness, which ensures that the contact area with the heater is fixed. Furthermore, since the thickness is the same, we assume that the thermal

doi:10.6342/NTU202302600

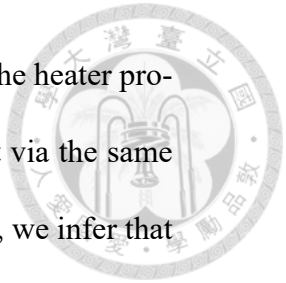

conductivity of the NiCu layer is also the same. Most importantly, the heater provides heat at the same power, which fixes the temperature gradient via the same power of heat flow and thermal conductivity. With these conditions, we infer that V_{ISHE} can be obtained directly from $V_{YIG} - V_{Si}$.

4.4 Spin Nernst Effect Measurement

As mentioned, there are few experiment research on spin Nernst effect since the signal is very small comparing with SMR. From the formula eq.2.18, spin Hall angle plays an important rule in the signal, which represent the ISHE process. With the large spin Hall angle which is comparable to heavy metals, we expect a clear observation of SNE and high efficiency of heat-to-spin conversion in NiCu.

4.4.1 Experiment Setup

In order to measure SNE, the sample holder is designed quite delicately, as shown in Fig.4.8. Heater and heat sink are located at a copper block. The former is separated from the block, while the latter is in contact with it. This makes it harder to dissipate heat from the heater, and easier for the heat sink to dissipate the heat. To realize the in-plane temperature gradient, a long strip sample is bridged on heater and heat sink. In addition, capping on two end which contact to heater and sample are necessary to reduce the out-of-plane temperature gradient. This uncontrollable heat flow cause extra signal. A silica pad and thermal grease with high thermal

doi:10.6342/NTU202302600

conductivity are applied to enhance the contact and thermal conduction.

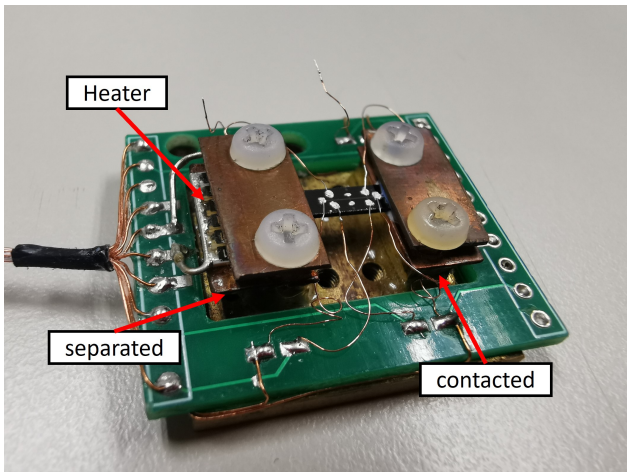

Figure 4.8: Sample holder used in SNITP measurement

Noise is the most difficult problem to solve in the process of experiment. Usually, the noise level is about $0.1\mu V$ for 2 probe contacted with sample which is much smaller than the MR signals we have measured. Light also gives noise, while being stable and low. However, these noise has a great influence on the SNE measurement. Recent research on Ta, W [10] and PT [11] has shown their result that the signal they measured has a level about $10nV$ to $0.5\mu V$, which is same or ever smaller then the noise. This makes it indistinguishable between signal and noise. Additionally, we also found other source of noise while doing experiment. In our experimental equipment, chiller cool down the electromagnet when it operating, creating ground shaking when the compressor start up. To make matters worse, air flow has a large influence on thermal transport measurement. It makes the temperature gradient unstable, which also affect the thermal voltage.

In [10], the author did not mention how they solve noise problem. But the

doi:10.6342/NTU202302600

SNE signal in W (Fig.2.10) is so large that the noise does not affect. It isn't lucky as W that signal in Ta is too low to distinguish. On the contrary, [11] measure Pt/YIG (Fig.2.11) in a cryostat giving vacuum environment. Comparing with two results, we see that although Pt has smaller signal than W, the SNE signal is observed clearly. Thus, isolated environment can solve the noise problem during the measurement.

There is no vacuum chamber which is small enough to fit the electromagnet in our experimental equipment. Instead, we use a cylinder made from aluminum foil by handmade. This also build an isolated environment. The performance of signal become better when applying in-plane field.

4.4.2 Pt/YIG

The measurement of SNITV is structurally similar to that of SMR. The only difference is the way how spin current is generated. Scanning field along x, y, and z direction to obtain the thermal voltage difference is an appropriate method to observe spin Nernst effect in Pt. On the other hand, sweeping angle doesn't work well, causing by the movement which affect thermal equilibrium.

The SNITV behavior with magnetic field scan for Pt(3 nm)/YIG sample is shown in Fig.4.9. Some of the features in SMR result also appears: saturation at specific field, curves contacting at low field, and the plateau in y direction curve. The only difference is that the curve is upside down, which implies $\theta_{SH}, (\theta_{SH} -$

doi:10.6342/NTU202302600

θ_{SN}), or Seebeck coefficient S is negative, which can be seen from eq.2.18.

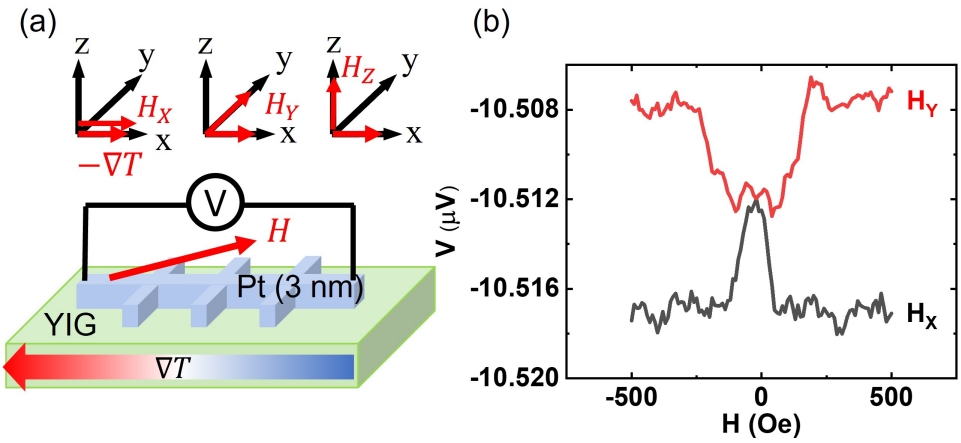

Figure 4.9: (a) Schematic diagram for thermal electric measurement in field scan method (b)Field dependence SNITP in Pt (3 nm)/YIG

In Fig.4.9, only symmetric part of signal be shown. Referring the SMR result, the curves have symmetric feature. Since the signal only depend on whether the magnetic moment parallel to direction of spin or not. It is equal under $+y$- and $-y$-direction field. Similar structure to SNITP measurement, we expect that the SNE signal is also symmetric. However, from the raw data in Fig.4.10, there is only the anti-symmetric feature, which is similar to SSE measurement result (Fig.4.7). We assume that the signal contain not only SNE but also a large part of SSE. We separate the symmetric part which represent SNITP from raw data by a simple process

$$V_{sym} = \frac{1}{2}(V_{raw,i}(H) + V_{raw,d}(-H)) \tag{4.4}$$

and the anti-symmetric part which represent SSE

$$V_{asym} = \frac{1}{2}(V_{raw,i}(H) - V_{raw,d}(-H)) \tag{4.5}$$

doi:10.6342/NTU202302600

where $V_{raw,i}(H)$ and $V_{raw,d}(H)$ represent the curve with increasing and decreasing field scan, respectively.

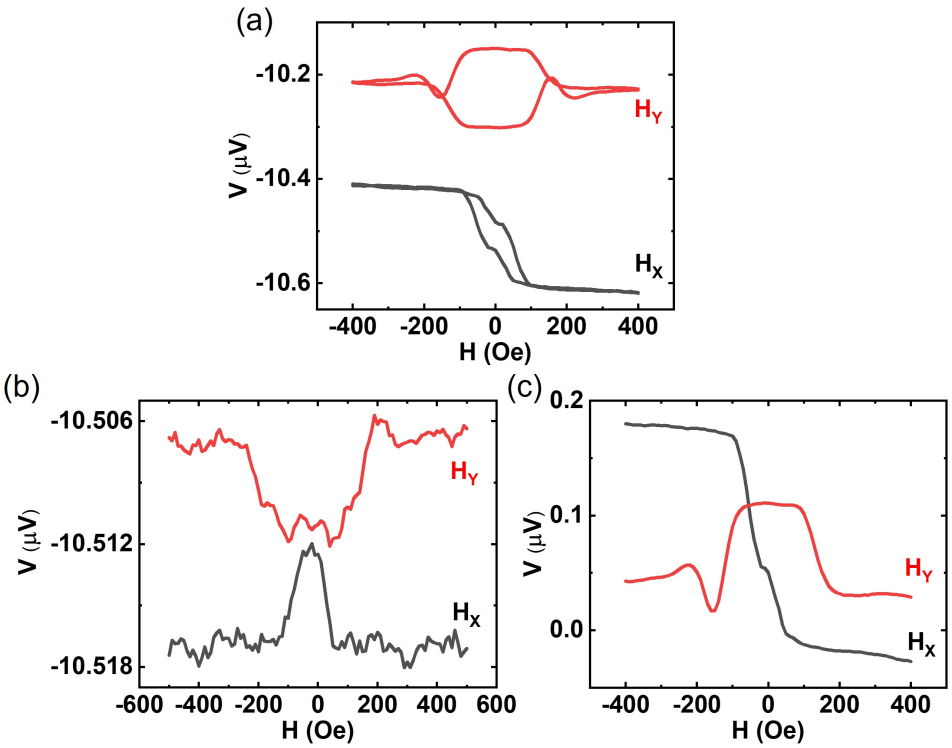

Figure 4.10: (a) Raw Data, (b) Symmetric, and (c) Asymmetric Part of Data

Even though we try to reduce the out-of-plane temperature by a capping, it cannot be completely eliminated. In Fig.4.11, we see that in our measurement setup, out-of-plane temperature gradient present at both ends of the sample with opposite direction. If we measure the transverse voltage under x direction field, we may find the SSE signal which is opposite in two terminals. This makes anti-symmetric signal appear when measure the SNITP in x direction field if there is miss alignment for the probe. On the other hand, despite the inhomogeneous out-of-plane temperature gradient, the SSE signal is also measured under the y

doi:10.6342/NTU202302600

direction field. Thus, separating the symmetric signal is an important process in SNE analysis.

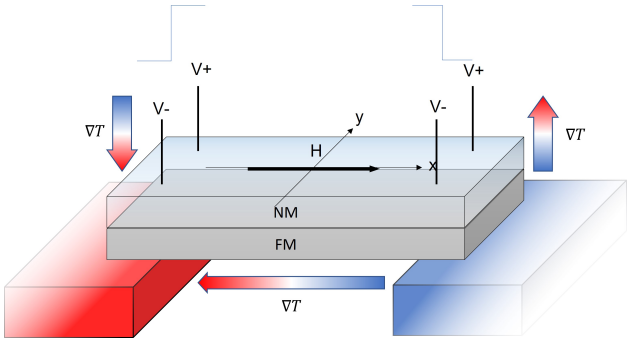

Figure 4.11: Schematic Diagram of Heat Flow.

To obtain the spin Nernst angle, we choose the voltage difference in black and red curves in 4.9 (b) and divide by the Seebeck voltage, which has

$$\frac{\Delta V_{XX}}{V_{XX}^{Z}} = \frac{V_{XX}^{Y} - V_{XX}^{X}}{V_{XX}^{X}} = 1.64 \times 10^{-3} \tag{4.6}$$

Choosing spin Hall angle $\theta_{SH} = 0.018$, spin diffusion length $\lambda_S = 1.5nm$, spin mixing conductance $G_{\uparrow\downarrow} = 4 \times 10^{14}\Omega^{-1}cm^{-2}$ [28]. Take into eq.2.18, we have the value of spin Nernst angle $\theta_{SN}^{0} = -18.0\%$, which is consistent with the result from [11].

Consistency indicate that the measuring system and the data analyze method is adaptable for SNE measurement. Under this definition of spin Nernst angle, the result is obtained by measuring voltage difference under the temperature gradient directly. However, heat flow create thermal voltage in metals. The phenomena is known as Seebeck effect. This voltage induce spin current by SHE, which gives additional signal. To estimate the efficiency of heat-to-spin conversion only from

doi:10.6342/NTU202302600

heat flow, the spin Nernst angle is redefined as

$$\frac{\Delta V_{XX}}{V_{XX}^{Z}} = \theta_{SH}(\theta_{SH} - \theta_{SN})\frac{\lambda_S}{d_N}\,\mathrm{Re}\left\{\frac{2\lambda_S G_{\uparrow\downarrow}\tanh^2\frac{d_N}{2\lambda_S}}{\sigma_C + 2\lambda_S G_{\uparrow\downarrow}\coth\frac{d_N}{\lambda_S}}\right\} \tag{4.7}$$

which subtract the unintentional E field contribution induced by Seebeck effect. Under this definition, the value of spin Nernst angle is $\theta_{SN} = -16.1\%$ being little different from the previous definition.

4.4.3 NiCu/YIG

Finally, the SNE measurement result for NiCu(10nm)/YIG sample is shown in Fig.4.12. We can see some feature similar to SMR result, including the plateau and negative field dependent voltage. As mentioned, the ratio may fixed in large field, which do not affect the result in spin Nernst angle. The only question is what the voltage difference. It is not clear whether the signal with field in z direction will exceed that with y as field getting larger. In Fig.4.13, we see that two curve contact together in large field. This means that the spin Nernst angle is zero under the first definition, referring the eq.2.18.

Let's recap. The strong spin-orbit coupling is confirmed, so there must be at least a spin current generated by heat flow in $Ni_{80}Cu_{20}$. Coupled with its own spin fluctuation to enhance the spin current. So the result of 0 is completely different from what we expected.

Comparing the Seebeck voltage with Pt, the $Ni_{80}Cu_{20}$ has higher efficiency of heat-to-charge conversion. Under same temperature gradient, Pt and $Ni_{80}Cu_{20}$ has

doi:10.6342/NTU202302600

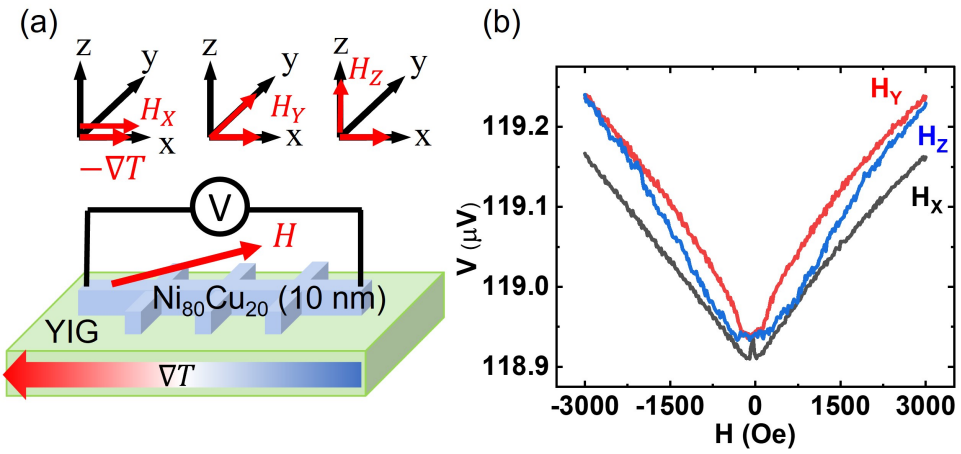

Figure 4.12: (a) Schematic diagram for thermal electric measurement in field scan method (b)Field dependence SNITP in $Ni_{80}Cu_{20}$ (10 nm)/YIG

Seebeck voltage of -10.5 μV and 119.0 μV, respectively. Thus the unintentional E field contribution has a great influence. Taking into the definition from eq.4.7, the spin Nernst angle is 12%. Different from Pt, spin Nernst angle of $Ni_{80}Cu_{20}$ has a same sign with spin Hall angle. Its value is also comparable with that of heavy metal, indicating the high efficiency of heat-to-spin conversion.

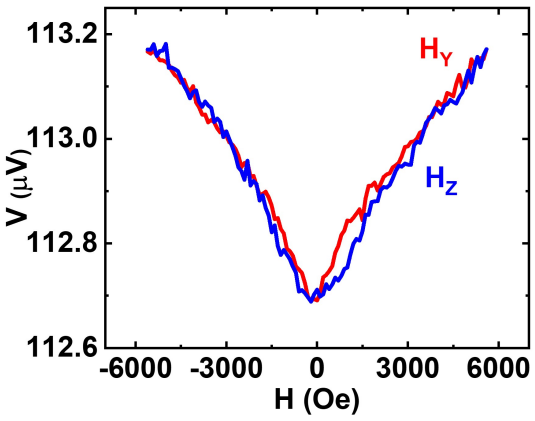

Figure 4.13: Field dependence SNITP in $Ni_{80}Cu_{20}$/YIG under large field

doi:10.6342/NTU202302600

doi:10.6342/NTU202302600

Chapter 5 Summary

The use of pure spin current as a means of transmitting information has gained considerable attention in recent years.

In this thesis, we investigate the properties of $Ni_{80}Cu_{20}$ alloy as a potential candidate for spintronic applications. By employing the inverse spin Hall effect, it has been confirmed that the NiCu alloy has an extremely large spin-to-charge conversion with spin Hall angle of $\theta_{SH} = 11\%$ in the ferromagnetic states, which is comparable with heavy metals.

To measure the spin current generated by the spin Nernst effect, we first measure the spin Hall magnetoresistance using a $Ni_{80}Cu_{20}$/YIG heterostructure to confirm the conversion of charge to spin. We obtain a spin Hall angle of $\theta_{SH} = 12\%$, which is consistent with previous study. Next, we measure the spin Nernst induced thermal voltage to obtain the spin Nernst angle. We develop an experimental apparatus that provides an in-plane temperature gradient and a method to separate the spin Nernst effect signal from raw data. We also solve the noise problem, resulting in higher resolution. The spin Nernst angle is determined to be $\theta_{SN} = 12\%$, which is consistent with the θ_{SH} measured by SMR and SSE measurement. At the same time, heat to charge conversion is known to have high efficiency through thermal voltage measurement. Therefore, our result indicates a large inter-conversion

doi:10.6342/NTU202302600

property between heat, spin and charge in $Ni_{80}Cu_{20}$ alloy.

	$S\ (\mu V/K)$	θ_{SH}	θ_{SN}
Pt	-0.93	0.018	-0.16
$Ni_{80}Cu_{20}$	-11.43	0.12^{*}, 0.14^{**}	0.12

Table 5.1: Conversion efficiency of Pt and $Ni_{80}Cu_{20}$. The absolute Seebeck coefficient is obtained from the relative Seebeck coefficient subtracted from the Cu Seebeck coefficient [31]. The spin Hall angle with superscript $*$ and $**$ is obtained from SMR and SSE+ISHE, respectively.

While this result is promising, further verification is needed to confirm. Nonetheless, our experimental setup and techniques provide a framework for investigating the spin Nernst effect in other materials and for advancing the field of spintronics.

doi:10.6342/NTU202302600

References

[1] D.D. Tang and C.F. Pai. *Magnetic Memory Technology: Spin-transfer-Torque MRAM and Beyond*. Wiley, 2021.

[2] Sabpreet Bhatti, Rachid Sbiaa, Atsufumi Hirohata, Hideo Ohno, Shunsuke Fukami, and S.N. Piramanayagam. Spintronics based random access memory: a review. *Materials Today*, 20(9):530–548, November 2017.

[3] M.I. Dyakonov and V.I. Perel. Current-induced spin orientation of electrons in semiconductors. *Physics Letters A*, 35(6):459–460, July 1971.

[4] T. Jungwirth, Qian Niu, and A. H. MacDonald. Anomalous hall effect in ferromagnetic semiconductors. *Phys. Rev. Lett.*, 88:207208, May 2002.

[5] Yan Sun, Yang Zhang, Claudia Felser, and Binghai Yan. Strong intrinsic spin hall effect in the taas family of weyl semimetals. *Phys. Rev. Lett.*, 117:146403, Sep 2016.

[6] Ke Tang, Yong-Chang Lau, Kenji Nawa, Zhenchao Wen, Qingyi Xiang, Hiroaki Sukegawa, Takeshi Seki, Yoshio Miura, Koki Takanashi, and Seiji Mitani. Spin hall effect in a spin-1 chiral semimetal. *Phys. Rev. Res.*, 3:033101, Jul 2021.

doi:10.6342/NTU202302600

[7] Ken ichi Uchida, Hiroto Adachi, Takeru Ota, Hiroyasu Nakayama, Sadamichi Maekawa, and Eiji Saitoh. Observation of longitudinal spin-seebeck effect in magnetic insulators. *Applied Physics Letters*, 97(17):172505, October 2010.

[8] K. Uchida, J. Xiao, H. Adachi, J. Ohe, S. Takahashi, J. Ieda, T. Ota, Y. Kajiwara, H. Umezawa, H. Kawai, G. E. W. Bauer, S. Maekawa, and E. Saitoh. Spin seebeck insulator. *Nature Materials*, 9(11):894–897, September 2010.

[9] Víctor H. Ortiz, Michael J. Gomez, Yawen Liu, Mohammed Aldosary, Jing Shi, and Richard B. Wilson. Ultrafast measurements of the interfacial spin seebeck effect in au and rare-earth iron-garnet bilayers. *Phys. Rev. Mater.*, 5:074401, Jul 2021.

[10] Peng Sheng, Yuya Sakuraba, Yong-Chang Lau, Saburo Takahashi, Seiji Mitani, and Masamitsu Hayashi. The spin nernst effect in tungsten. *Science Advances*, 3(11):e1701503, 2017.

[11] S. Meyer, Y.-T. Chen, S. Wimmer, M. Althammer, T. Wimmer, R. Schlitz, S. Geprägs, H. Huebl, D. Ködderitzsch, H. Ebert, G. E. W. Bauer, R. Gross, and S. T. B. Goennenwein. Observation of the spin nernst effect. *Nature Materials*, 16(10):977–981, Oct 2017.

[12] Po-Hsun Wu, Danru Qu, Yen-Chang Tu, Yin-Ze Lin, C. L. Chien, and Ssu-Yen Huang. Exploiting spin fluctuations for enhanced pure spin current.

doi:10.6342/NTU202302600

Phys. Rev. Lett., 128:227203, Jun 2022.

[13] S. M. Rezende, R. L. Rodríguez-Suárez, R. O. Cunha, A. R. Rodrigues, F. L. A. Machado, G. A. Fonseca Guerra, J. C. Lopez Ortiz, and A. Azevedo. Magnon spin-current theory for the longitudinal spin-seebeck effect. *Phys. Rev. B*, 89:014416, Jan 2014.

[14] Yaroslav Tserkovnyak, Arne Brataas, and Gerrit E. W. Bauer. Enhanced gilbert damping in thin ferromagnetic films. *Phys. Rev. Lett.*, 88:117601, Feb 2002.

[15] J. E. Hirsch. Spin hall effect. *Phys. Rev. Lett.*, 83:1834–1837, Aug 1999.

[16] Jairo Sinova, Sergio O. Valenzuela, J. Wunderlich, C. H. Back, and T. Jungwirth. Spin hall effects. *Rev. Mod. Phys.*, 87:1213–1260, Oct 2015.

[17] Dong-Jun Kim, Chul-Yeon Jeon, Jong-Guk Choi, Jae Wook Lee, Srivathsava Surabhi, Jong-Ryul Jeong, Kyung-Jin Lee, and Byong-Guk Park. Observation of transverse spin nernst magnetoresistance induced by thermal spin current in ferromagnet/non-magnet bilayers. *Nature Communications*, 8(1), November 2017.

[18] T. Wimmer, J. Gückelhorn, S. Wimmer, S. Mankovsky, H. Ebert, M. Opel, S. Geprägs, R. Gross, H. Huebl, and M. Althammer. Low-temperature suppression of the spin nernst angle in pt. *Phys. Rev. B*, 104:L140404, Oct 2021.

[19] E. Saitoh, M. Ueda, H. Miyajima, and G. Tatara. Conversion of spin current

doi:10.6342/NTU202302600

into charge current at room temperature: Inverse spin-hall effect. *Applied Physics Letters*, 88(18):182509, May 2006.

[20] T. Kimura, Y. Otani, T. Sato, S. Takahashi, and S. Maekawa. Room-temperature reversible spin hall effect. *Phys. Rev. Lett.*, 98:156601, Apr 2007.

[21] D. Qu, S. Y. Huang, B. F. Miao, S. X. Huang, and C. L. Chien. Self-consistent determination of spin hall angles in selected $5d$ metals by thermal spin injection. *Phys. Rev. B*, 89:140407, Apr 2014.

[22] Yan-Ting Chen, Saburo Takahashi, Hiroyasu Nakayama, Matthias Althammer, Sebastian T. B. Goennenwein, Eiji Saitoh, and Gerrit E. W. Bauer. Theory of spin hall magnetoresistance. *Phys. Rev. B*, 87:144411, Apr 2013.

[23] H. Nakayama, M. Althammer, Y.-T. Chen, K. Uchida, Y. Kajiwara, D. Kikuchi, T. Ohtani, S. Geprägs, M. Opel, S. Takahashi, R. Gross, G. E. W. Bauer, S. T. B. Goennenwein, and E. Saitoh. Spin hall magnetoresistance induced by a nonequilibrium proximity effect. *Phys. Rev. Lett.*, 110:206601, May 2013.

[24] Tomohiro Taniguchi. Phenomenological spin transport theory driven by anomalous nernst effect. *Journal of the Physical Society of Japan*, 85(7):074705, July 2016.

[25] Chi Sun, S M Rafi-Ul-Islam, Hyunsoo Yang, and Mansoor B. A. Jalil. Spin

doi:10.6342/NTU202302600

nernst and anomalous nernst effects and their signature outputs in ferromagnet/nonmagnet heterostructures. *Phys. Rev. B*, 102:214419, Dec 2020.

[26] Naoto Nagaosa, Jairo Sinova, Shigeki Onoda, A. H. MacDonald, and N. P. Ong. Anomalous hall effect. *Rev. Mod. Phys.*, 82:1539–1592, May 2010.

[27] Po-Hsun Wu, Ying-Ting Chan, Tzu-Chao Hung, Yi-Hui Zhang, Danru Qu, Tien-Ming Chuang, C. L. Chien, and Ssu-Yen Huang. Effect of demagnetization factors on spin current transport. *Phys. Rev. B*, 102:174426, Nov 2020.

[28] Sibylle Meyer, Matthias Althammer, Stephan Geprägs, Matthias Opel, Rudolf Gross, and Sebastian T. B. Goennenwein. Temperature dependent spin transport properties of platinum inferred from spin hall magnetoresistance measurements. *Applied Physics Letters*, 104(24):242411, 2014.

[29] Amelia Carolina Sparavigna. Thermal Conductivity of the Crystalline Silicon. *Philica*, page 1143, 2017.

[30] D. R. Ratkovski, L. Balicas, A. Bangura, F. L. A. Machado, and S. M. Rezende. Thermal transport in yttrium iron garnet at very high magnetic fields. *Phys. Rev. B*, 101:174442, May 2020.

[31] William M. Haynes, editor. *CRC Handbook of Chemistry and Physics*. CRC Press, June 2014.

doi:10.6342/NTU202302600